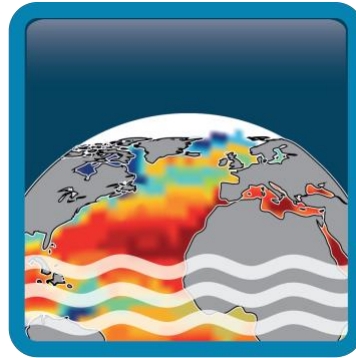


Climate Change Initiative+ (CCI+) Phase 2

Sea Surface Salinity



[D2.3] Algorithm Theoretical Development Basis Document (ATBD)

Customer: ESA

Ref.: ESA-CCI-PRGM-EOPS-SW-17-0032

Version: v4.0

Ref. internal: AO/1-9041/17/I-NB_v4r0






Revision Date: 15/07/2023

Filename: SSS_cci-D2.3-ATBD-v4.0

Deliverable code: D2.3



Signatures

Author	Jean Luc Vergely		15-07-2023
Author	Nicolas Reul		1-09-2023
Author	Meriem Chakroun		14-09-2021
Reviewed by	Rafael Catany		
	Paolo Cipollini		
Approved by	Jacqueline Boutin (Science Leader)		14-09-2021
	Nicolas Reul (Science Leader)		14-09-2021
	Rafael Catany (Project Manager)		14-09-2021
Accepted by	Roberto sabia (Technical Officer)		

Diffusion List
Sea Surface Salinity Team Members
ESA (Craig Donlon, Paolo Cipollini)

Amendment Record Sheet

Date / Issue	Description	Section / Page
15-07-2019 / v1.0	Delivery to ESA	New Document
22-10-2019 / v1.2	Update reference document documents section	
	Updated acronym table	
	Improved text in captions of Figures: 5-9	
	Rephrasing main text	
	Updated text in caption of Figure: 5-9	
30-04-2020/v2.0	Updated L2,L3 and L4 Algorithm	
24/06/2020/v2.1	Added feedback/suggestions as provided by ESA (minor)	N/A
19/07/2021/v3.0	Phase 1 final version	All
14/09/2021/v3.1 (this document)	Minor formatting editions for delivery	N/A
15/07/2023/v4.0	First delivery for phase 2	

Table of Contents

1	Introduction	12
1.1	Scope of this document	12
1.2	Structure of the document	12
1.3	References	12
1.3.1	Applicable Documents	12
1.3.2	Reference Documents	13
1.4	Acronyms	15
2	L-band SSS retrieval algorithm	17
2.1	Level 2 Algorithms	17
2.1.1	Introduction	17
2.1.2	Input data for L4 CCI+SSS estimation	18
2.2	Level 4 algorithms	19
2.2.1	Introduction	19
2.2.2	L4 algorithm	22
3	Conclusions and way forward for L-band sensor Algorithm.....	33
4	AMSR-E C- and X-band SSS retrieval Algorithm.....	34
4.1	SSS retrieval Algorithm Overview	34
4.1.1	Historical Background and general approach	34
4.1.2	AMSR-E sensor and characteristics	38
4.1.3	Algorithm Overview	41
4.2	Input data for CCI+SSS from AMSR-E C/X-bands	44
4.2.1	AMSR-E/Aqua L2A Global Swath Spatially-Resampled Brightness Temperatures.....	44
4.2.2	AMSR-E/Aqua L2B Global Swath Ocean Products.....	44
4.2.3	Sea Surface Temperature Climate Change Initiative Products	44
4.3	Radiative Transfer Model (RTM)	45
4.3.1	Top of the Atmosphere Brightness temperature	45
4.3.2	Atmospheric contributions	46
4.3.3	Sea Surface Emission	51
4.3.4	Atmospheric and cosmic Radiation Scattered by the Sea Surface.....	59
4.3.5	Frequency differential specular sea surface emissivity contrast	60
4.4	AMSR-E SSS retrieval Algorithm	61
4.4.1	Input Data Filtering	61
4.4.2	Input Data re-gridding	65
4.4.3	Surface specular V-pol brightness temperature at C- and X-band	65
4.4.4	Earth Incidence Variations.....	65
4.4.5	SST and Atmospheric corrections refinements	65
4.4.6	Outliers Removal	70
4.4.7	Neural Network SSS inversion	73
4.4.8	References for AMSR-E SSS algorithm	75
5	Conclusions and way forward for AMSR-E SSS algorithm	77
Appendix A - L2P algorithms.....		79
A.1	Introduction.....	79
A.2	Method.....	79
A.2.1	Input Data re-gridding	79
A.2.2	L2P variables definition	79
A.3	Conclusion	81
Appendix B - L3C algorithms.....		82

B.1	Introduction.....	82
B.2	Input data for CCI+SSS L3 data	82
B.2.1	SMOS and SMAP L2P products	82
B.2.2	Aquarius Level 3 products	82
B.3	CCI+SSS L3 product overview	82
B.4	Method.....	83
B.4.1	Input Data re-gridding	83
B.4.2	Input Data correction	83
B.4.3	Data filtering	83
B.4.4	L3C variables definition	84
B.5	Conclusion	86

List of figures

Figure 1:main L4 processing steps. -----	22
Figure 2: Examples of climatological maps of monthly SSS variability relative to the whole period SSS mean, that are considered in the optimal interpolation. a) February; b) May; c) August; d) November. -----	24
Figure 3: Principle of the self-consistency approach. Example of a grid point near the Amazon plume (48°W, 5.2°N) affected by land sea contamination, seen under various satellite geometry during ascending orbits (SMOS L2 SSS, left hand side of the FOV, green points; SMAP L2 SSS, aft antenna, red points; Aquarius L3 daily SSS, blue points). a) Satellite SSS before correction (SSS_{obs}) and SSS_{ref} (black line) ; b) Satellite SSS after relative adjustment ($SSS_{rel}+SSS_{ref}$) and SSS_{ref} (black line); c) Satellite SSS after relative adjustment ($SSS_{rel}+SSS_{ref}$), weekly OI relative SSS (black) and ISAS SSS (light blue); d) Same as c) but after absolute calibration of the weekly OI SSS by adjusting the 80% quantile of the weekly OI SSS statistical distribution to that of the ISAS SSS. -----	26
Figure 4: Quantile map used for the SSS absolute calibration. x and y axis units in pixel number for longitude and latitude respectively. -----	30
Figure 5: Sketch showing the different satellites operating low-microwave frequency radiometers characteristics from which SSS remote sensing from Space can be estimated in the modern satellite era. Along the timeline, C-band sensors are shown in orange while L-band ones are in blue. -----	34
Figure 6: Spatial Domain of the regional AMSR-E based SSS products developed for the CCI project -----	35
Figure 7 Sensitivity of the flat ocean brightness temperature to SSS, namely, $\partial TB/\partial SSS$ as a function of electromagnetic frequency (x-axis) computed from Klein and Swift (1977) for the salinity of 35 psu and temperature of 15°C with a fixed incident angle of 53°. -----	36
Figure 8 Brightness temperature of the flat sea surface in microwave bands as functions of SSS (y-axis) and SST(x-axis). (a) brightness at 6.9 GHz (C band) (b) Brightness at 10.7 GHz (X band) in V-pol and (c) brightness temperature difference between the 10.7 GHz and 6.6 GHz in V-pol. 37	
Figure 9: Change of the differential flat ocean surface brightness temperature with SSS for fixed values of SSS (left) and with SST for fixed values of SSS (right). -----	37
Figure 10: Sketch showing the flow of the AMSR-E SSS retrieval -----	41
Figure 11: Meissner and Wentz's (2012) model of the effective air temperature for upwelling TD and downwelling TU radiation as a function of the vertically integrated Columnar water vapor V . The curves are provided for both C- and X- band frequencies -----	49
Figure 12: Isotropic components of the wind-induced emission at C- and X-band and Vertical Polarization -----	56
Figure 13: GMF of the first (left) and second (right) azimuthal harmonic coefficients $\Delta e_1, VU_{10}$ as a function of surface wind speed for L- (blue), C-(black) and X-(red) bands.. The values have been multiplied by a common surface temperature of 290 K. -----	58

Figure 14: Redidual Biases between estimated specular sea surface emission from AMSR-E and forward model estimates (based on CCI SSS and SST) as a function of CCI SST for C-band (left) and X-band (right) at V-polarized data. The blue curves are showing the median bias ± 1 STD as a function of the SST. The red curves are 6th-order polynomial fits. ----- 66

Figure 15: Observed (left plots) and modeled (right plots) residual biases as a function of both columnar Water Vapor (V) and Cloud liquid water (L). Top and bottom panels are for C- and X-band corrections, respectively.----- 68

Figure 16: median absolute temporal deviation (MAD) of the specular sea surface emissivity frequency differential contrasts $\Delta esurf_{spec}$ for the Amazon region. The high MAD in the north is due to high WV impacts. ----- 71

List of tables

Table 1. Missions characteristics-----	17
<i>Table 2 Aqua/AMSR-E Instrument characteristics compared to L-band satellite radiometers ---</i>	38
Table 3: Isotropic roughness emissivity coefficients a_{oi}, V for the C- and X-band frequencies and V polarization-----	56
Table 4: First azimuthal harmonic coefficients a_{1i}, p for the C- and X-band frequencies and V-polarization -----	57
Table 5: Second azimuthal harmonic coefficients a_{2i}, p for the C- and X-band frequencies and V-polarization -----	57
Table A-1: L2P definition extracted from processing level of CCI Data Standards document [AD.9]. -----	79
Table B-1: L3C definition extracted from processing level of CCI Data Standards document [AD.9]. -----	83



1 Introduction

1.1 Scope of this document

Sea Surface Salinity (SSS) is an Essential Ocean and Climate Variable, which is increasingly used as part of climate studies. SSS measurements are available from three satellite missions, SMOS, Aquarius and SMAP, each with very different instrument features leading to specific measurement characteristics. The Climate Change Initiative Salinity project (CCI+SSS) aims to produce SSS Climate Data Record (CDR) to include satellite measurements, based on well-established user needs. To generate a homogeneous CDR, instrumental differences are carefully controlled by analysing SSS discrepancies, then adjusted based on in-depth analysis of the measurements themselves together with independent reference data. However, no spatial smoothing or temporal relaxation to reference data is applied in order to maintain the variability contained in the original data set. This document gives details on the algorithms used for CDR generation. It holds the Algorithm Theoretical Development Basis Document (ATBD) prepared by CCI+SSS team, as part of the activities included in the [WP230] of the Proposal (Task 2 from SoW ref. ESA-CCI-PRGM-EOPS-SW-17-0032).

1.2 Structure of the document

This document (ATBD v4.0) is composed of 4 sections and presents the CCI+SSS algorithms implemented in the third version of the products (products delivered at the end of the phase 1). Section 1 is an introduction presenting the scope, reference and applicable documents, acronyms, and the structure of the ATBD. Section 2 presents the algorithms of the so-called Level 2 products which are swath retrievals from L-band sensor SMOS. Section 3 presents the Level 3 SSS products, which are averaged intermediate products obtained sensor by sensor, without mixing inter-sensor information. Level 4 data set, produced each year, form the core of the CCI+SSS products and is described in §4. In Section 5, we provide summary and discuss the perspectives. The Annex presents the L2 and L3 algorithms.

1.3 References

1.3.1 Applicable Documents

ID	Document	Reference
AD01	Sea Surface Salinity Climate Change Initiative Phase 1 Data Access Requirement Document.	SSS_cci-D1.3-DARD-v1r4
AD02	SMOS Level2 Algorithm Theoretical Baseline Document (ATBD). Available at: https://earth.esa.int/documents/10174/1854519/SMOS_L2OS-ATBD	SO-TN-ARG-GS-0007_L2OS-ATBD v3.13



**Climate Change Initiative+ (CCI+)
Phase 2**

**Algorithm Theoretical
Development Basis Document**

Ref.: ESA-CCI-PRGM-EOPS-SW-17-0032

Date: 15/07/2023

Version : v4.0

Page: 13 of 87

ID	Document	Reference
AD03	CATDS (2017). CATDS-PDC L3OS 2P Algorithm Theoretical Basis Document. Available at: https://www.catds.fr/content/download/78841/file/ATBD_L3OS_v3.0.pdf	ATBD_L3OS_v3
AD04	Aquarius Official Release Level 2 Sea Surface Salinity v5.0 ATBD. Available at: ftp://podaac-ftp.jpl.nasa.gov/allData/aquarius/docs/v5/	RSS Technical Report 120117
AD05	Aquarius Official Release Level 3 Sea Surface Salinity v5.0. Aquarius L2 to L3 Processing Document. ATBD. Available at: ftp://podaac-ftp.jpl.nasa.gov/allData/aquarius/docs/v5/	AQ-014-PS-0017_Aquarius_L2toL3ATBD_DatasetVersion5.0
AD06	RSS SMAP Level 2 Sea Surface Salinity V3.0 40km Validated Dataset. Available at: ftp://podaac-ftp.jpl.nasa.gov/allData/smap/docs/V3/	RSS Technical Report 101518
AD07	Sea Surface Salinity Climate Change Initiative Phase 1 Product Specification Document	SSS_cci-D1.2-PSD-v1r6
AD08	Sea Surface Salinity Climate Change Initiative Phase 1 Algorithm Theoretical Development Basis Document	SSS_cci-D2.5-PVP-v1.0
AD09	CCI Data Standards	CCI-PRGM-EOPS-TN-13-0009
AD10	Sea Surface Salinity Climate Change Initiative Phase 1 End-to-End ECV Uncertainty Budget (E3UB)	SSS_cci-D2.3-E3UB-v1.2
AD11	NASA/RSS SMAP Salinity: Version 5.0 Validated Release, March 31, 2022	RSS Technical Report 033122
AD12	Sea Surface Salinity Climate Change Initiative Phase 2 End-to-End ECV Uncertainty Budget (E3UB)	SSS_cci-D2.3-E3UB-v4r0

1.3.2 Reference Documents

ID	Document	Reference
RD01	Boutin, J., N. Martin, N. Kolodziejczyk, and G. Reverdin (2016a), Interannual anomalies of SMOS sea surface salinity, <i>Remote Sensing of Environment</i>	doi:http://dx.doi.org/10.1016/j.rse.2016.02.053
RD02	Kolodziejczyk, N., J. Boutin, J.-L. Vergely, S. Marchand, N. Martin, and G. Reverdin (2016), Mitigation of systematic errors in SMOS sea surface salinity, <i>Remote Sensing of Environment</i>	doi:http://dx.doi.org/10.1016/j.rse.2016.02.061.
RD03	Liang Hong, Normal Kuring, Joel Gales and Fred Patt (2017), AQ-014-PS-0017_Aquarius_L2toL3ATBD_DatasetVersion5.0	



**Climate Change Initiative+ (CCI+)
Phase 2**

**Algorithm Theoretical
Development Basis Document**

Ref.: ESA-CCI-PRGM-EOPS-SW-17-0032

Date: 15/07/2023

Version : v4.0

Page: 14 of 87

ID	Document	Reference
RD04	Fred Patt, Liang Hong (2017), AQ-014-PS-0018_AquariusLevel2specification_DatasetVersion5.0	
RD05	Meissner, T. and F. J. Wentz, 2016: Remote Sensing Systems SMAP Ocean Surface Salinities [Level 2C, Level 3 Running 8-day, Level 3 Monthly], Version 2.0 validated release. Remote Sensing Systems, Santa Rosa, CA, USA.	www.remss.com/missions/smap , doi:10.5067/SMP20-2SOCS
RD06	Boutin J., J.-L. Vergely, S. Marchand, F. D'Amico, A. Hasson, N. Kolodziejczyk, N. Reul, G. Reverdin, J. Vialard (2018), New SMOS Sea Surface Salinity with reduced systematic errors and improved variability, <i>Remote Sensing Of Environment</i>	doi: http://dx.doi.org/10.1016/j.rse.2018.05.022
RD07	Yiwen Zhou ; Roger H. Lang ; Emmanuel P. Dinnat ; David M. Le Vine (2017), L-Band Model Function of the Dielectric Constant of Seawater, <i>IEEE Transactions on Geoscience and Remote Sensing</i> (Volume: 55 , Issue: 12)	
RD08	Gaillard F. (2015), ISAS-13 temperature and salinity gridded fields. SEANOE.	http://doi.org/10.17882/45945 .
RD09	Merchant, C. J., Paul, F., Popp, T., Ablain, M., Bontemps, S., Defourny, P., Hollmann, R., Lavergne, T., Laeng, A., de Leeuw, G., Mittaz, J., Poulsen, C., Povey, A. C., Reuter, M., Sathyendranath, S., Sandven, S., Sofieva, V. F., and Wagner, W.(2017), Uncertainty information in climate data records from Earth observation, <i>Earth Syst. Sci. Data</i> , 9, 511–527	https://doi.org/10.5194/essd-9-511-2017 , 2017
RD10	Boutin et al., Satellite-based Time-Series of Sea Surface Salinity designed for Ocean and Climate Studies, <i>JGR-Oceans</i> , in revision, 2021.	
RD11	Boutin, J., J.-L. Vergely, E. P. Dinnat, P. Waldteufel, F. D'Amico, N. Reul, A. Supply, and C. Thouvenin-Masson (2020), Correcting Sea Surface Temperature Spurious Effects in Salinity Retrieved From Spaceborne L-Band Radiometer Measurements, <i>IEEE Transactions on Geoscience and Remote Sensing</i> , 1-14, doi:10.1109/tgrs.2020.3030488.	
RD12	Klein, L., and C. Swift (1977), An improved model for the dielectric constant of sea water at microwave frequencies, <i>IEEE Transactions on Antennas and Propagation</i> , 25(1), 104-111.	



1.4 Acronyms

AD	Applicable Document
ATBD	Algorithm Theoretical Basis Document
Aquarius	Aquarius NASA/SAC-D sea surface salinity mission
BV	Boutin-Vergely sea water dielectric constant model
CCI	The ESA Climate Change Initiative (CCI) is formally known as the Global Monitoring for Essential Climate Variables (GMECV) element of the European Earth Watch programme
CCI+	Climate Change Initiative Extension (CCI+), is an extension of the CCI over the period 2017–2024
CMEMS	Copernicus Marine Environmental Monitoring Service
DARD	Data Access Requirements Document
DOI	Digital Object Identifier
DPM	Detailed Processing Model
ECMWF	European Centre for Medium Range Weather Forecasts
EASE	Equal-Area Scalable Earth (EASE) Grid
ECV	Essential Climate Variable
EO	Earth Observation
FOV	Field Of View
Hs	Significant Wave Height (see also SWH)
ISAS	In Situ Analysis System
KS	Klein and Swift sea water dielectric constant model
MW	Meissner and Wentz sea water dielectric constant model
NASA	National Aeronautics and Space Administration
NOAA	National Oceanic and Atmospheric Administration
NOP	Numerical Ocean Prediction



Climate Change Initiative+ (CCI+)
Phase 2

**Algorithm Theoretical
Development Basis Document**

Ref.: ESA-CCI-PRGM-EOPS-SW-17-0032

Date: 15/07/2023

Version : v4.0

Page: 16 of 87

NWP	Numerical Weather Prediction
OTT	Ocean Target Transform
SMAP	Soil Moisture Active Passive
SSS	Sea Surface Salinity
SST	Sea Surface Temperature
SWH	Significant Wave Height (see also Hs)
TBC	To Be Confirmed
UCR/CECR	Uncertainty Characterisation Report (formerly known as the Comprehensive Error Characterisation Report)
URD	User Requirements Document
VOS	Volunteer Observing ships
WS	Wind Speed



2 L-band SSS retrieval algorithm

2.1 Level 2 Algorithms

2.1.1 Introduction

In the second phase of the CCI+SSS project (April 2022 – July 2023), the generation of the L4 CCI+SSS dataset used input data at levels 2 (i.e. non averaged retrieved SSS along each satellite orbit) for SMOS and SMAP and Level 3 (i.e. daily ascending and descending orbits separately) for Aquarius sensor. These data are all projected on the same regular grid at a spatial sampling of 0.25°. A global product is given on this grid and two polar products are generated from global product interpolation (nearest neighbour interpolation) over two polar EASE2 grids (north and south) at 25km of resolution.

The SMOS L2 products come from DPGS (ESA center).

The SMAP L2 and Aquarius L3 products come from official space agency dedicated center (RSS). They are therefore not generated by the CCI+SSS processing chains.

The main characteristics of L-band radiometric satellite missions enabling global SSS measurements are summarized in **Table 1**.

Table 1. Missions characteristics

SMOS MISSION	AQUARIUS MISSION	SMAP MISSION
<i>Mission Characteristics</i>		
-L-band interferometry. 0°-~60° earth incidence angles -revisit times: 4 days -resolution: about 45 km -repeat sub-cycle: 18 days -see more in (Font et al., 2010; Y. Kerr et al., 2010)	-L-band real-aperture radiometer. 3 fixed beams at 28.7, 37.8, and 45.6° earth incidence angles -revisit times: 7 days -resolution: about 150 km -repeat cycle: 7 days -see more in (Lagerloef et al., 2008)	-L-band real-aperture radiometer. Conical scanning, 40° earth incidence angle -revisit times: 3 days -resolution: about 45 km -repeat cycle : 8 days -see more in (Piepmeier et al., 2017)
<i>Vicarious calibration</i>		
-Spatially constant and time-varying mean calibration: OTT: 10day mean differences in the	- Spatially constant and time-varying mean calibration: OTT: 7day mean differences over global ocean using	- Zonal calibration: emissive reflector correction to minimize orbital biases, estimated for each day of the year using



south-east Pacific Ocean using WOA 2009 SSS climatology.	Scripps Argo SSS (Meissner et al., 2018).	Scripps Argo SSS. It is the same for all years (Meissner et al., 2019) - Spatially constant and time-varying mean calibration: OTC: 3day mean differences over global ocean using Hycom SSS (Meissner et al., 2019). -specific processing (v5) for ice contamination mitigation.
<i>RFI filtering</i>		
Outlier detection performed in Level 2 processing.	Specific RFI detection (Le Vine and Matthaeis, 2014)	Specific RFI detection (Soldo et al., 2019)

2.1.2 Input data for L4 CCI+SSS estimation

2.1.2.1 Measurement products

SMOS Level 2

CCI SMOS L2 reprocessing has been performed over the period [01/2010-10/2022] by using SMOS L2 products. The L1 products used as input correspond to the v7 L1c processed by the DPGS which include gibbs2 algorithm.

SMOS level 2 corresponds to ESA v700 L2OS products.

SMAP Level 2

In CCI V4, we directly use as input SMAP RSS Level 2 v5.0 products. These are provided daily at 40 km resolution. The data are split into ascending and descending products and between the fore and aft views. Details on the processing algorithms can be found in [AD06] and [AD11].

Aquarius Level 3

Aquarius acquisitions present heterogeneous sampling according to latitude and longitude. Also, the zonal and meridian resolution is not homogeneous. In order to use the Aquarius data, it is therefore necessary to carry out a first spatial homogenization of the data. RSS offers such an L3 product which distinguishes ascending and descending orbits and which is given on a regular grid at 1°. In view of the results of the first versions an analysis has shown that Aquarius had too



much weight in the error budget which generated too smooth L4 products. In order to give more weight to the other sensors, the error on the Aquarius data has been multiplied by 2. Note that a representativeness error is added to the Aquarius measurement error.

2.1.2.2 SST correction

An empirical correction depending on SST is applied for SMAP and Aquarius SSS (AD12).

For SMOS, BV constant dielectric model has been updated and a correction has been applied (AD12).

2.1.2.3 Regular grid projection

The choice of the CCI grid fell on the EASE rectangular regular 0.25° grid. Sampling in longitude and latitude is constant. Before aggregation, the SMOS, SMAP and Aquarius data must appear on the same grid. It is therefore a question of interpolating the salinities from one grid to another. For SMOS, the initial reconstruction grid is the ISEA 12 km grid. This is an oversampled grid at 12km resolution. The projection from the ISEA grid to the regular grid is done by nearest neighbors. For SMAP, originally on a 0.25° grid, we also proceed by closest neighbors because of small shift. For Aquarius, the closest neighbor approach is not recommended because, given the native grid resolution of 1°, this generates artificial constant SSS values on 1° per 1° tiles. To avoid this effect, a linear interpolation with a quadratic weighting according to the distance of the 4 nearest neighbors has been implemented. Moreover, if only three neighbors are available, the interpolation is carried out which avoids artificially removing information on the swath edges.

2.1.2.4 Representativity uncertainties and a priori variability.

The L4 salinity retrieval algorithm is an optimal Bayesian interpolation. This interpolation scheme needs as input the covariance of the a priori salinity field. This covariance is described in section 2.2.2.1. In addition, salinities coming from different sensors which have different spatial resolutions are mixed. In this situation, it is a matter of adding a representativity uncertainty to the measurement error. This representativity uncertainty also depends on the temporal smoothing (monthly or weekly). It is calculated from Mercator salinity fields.

2.2 Level 4 algorithms

2.2.1 Introduction

In order to merge the SSS of the different sensors, we start directly from the SMOS and SMAP L2 products and from the Aquarius L3 products as respectively described in section 2.1.2.1 after a projection on the 0.25° regular grid (section 2.1.2.3) and some additive corrections and filtering (see [AD12]).



Monthly and weekly maps of SSS are derived from the three satellite missions using a temporal optimal interpolation (OI). We do not apply any spatial smoothing so that the spatial resolution of each level 4 SSS is roughly $50 \times 50 \text{ km}^2$ over the 0.25° regular grid. We correct for systematic differences between the SSS from the various satellite missions acquired with different geometry as will be described below. We provide an uncertainty associated to the CCI L4 SSS product.

In the following, we describe the methodologies we follow to derive level 4 SSS fields, successively including:

- the optimal interpolation method,
- the characterization of the uncertainties on level 2 SSS derived from each satellite mission, linked to observational uncertainties (Vinogradova et al., 2019), (with a covariance matrix denoted C_d in the following).

The quantification of the SSS natural variability involved in:

- the representativity uncertainty, also called sampling uncertainty (Vinogradova et al., 2019), which originates from the different spatial resolutions of the various sensors, (with a covariance matrix denoted C_r in the following),
- the spatio-temporal variability relative to a mean value used to adjust the OI estimate (covariance matrix denoted C_2 in the following).

In order to estimate SSS at a given time, the algorithm is using an optimal interpolation. This interpolation is applied grid node per grid node, without spatial smoothing by merging temporally the SSS from the three sensors. Indeed, we want to preserve the spatial and temporal dynamics of the SSS and to avoid a spatial catch-up made to monthly reference climatological fields which might remove or attenuate important interannual and/or large mesoscale variations.

The approach adopted to generate Level 4 CCI+SSS products is as follows:

- The bias correction exploits as much information as possible from the data. SSS that seem to be affected by various contaminations (coastal, RFI, galactic, solar, etc.) are kept in our algorithm. It is considered that these contaminations can, to some extent, be corrected a posteriori, since in most cases these effects lead to systematic errors that can be confused with real geophysical signals. In fact, in some cases, satellite data provide information on strong geophysical signals that can reach several units in the Practical Salinity Scale (pss). In this situation, a bias in the order of the pss does not justify the removal of the data.
- The self-consistency of the measurements (averaged over a monthly time window) over the whole time period (2010-2022), and accounting for the natural variability of the SSS expected in this window, allows the different inter-sensor biases to be corrected relatively to each other. An a posteriori 3 sigma filtering is then applied to remove outliers. These filters are applied with respect to the natural SSS variability that must be taken into account in the satellite SSS estimation process. Indeed, if a low variability is expected (in comparison to SSS L2 retrieval error), the filters applied must be more



severe. Otherwise (e.g., at river mouths, or, in strong currents where natural SSS variability is high), data that differ significantly (from more than 3 times the retrieval error on the SSS) from the mean should be retained.

- The self-consistency criteria considered in the algorithms is temporal. A spatial correction of the SSS according to a certain reference (e.g. WOA climatology) could affect spatial and temporal dynamics and could remove some of the interannual signals and mesoscale signatures. This is why we didn't apply spatial correction. We therefore consider coastal/ocean biases that are constant over time. These biases can be corrected without affecting geophysical SSS dynamics. In practice, the SSS correction/estimation is done grid node per grid node considering the inter-sensor self-consistency in SSS. To correct for seasonal latitudinal biases, a relative correction is also applied on SMOS, SMAP L2 data and Aquarius L3 data, similar to what is described in Boutin et al (2018). It applies to all basins and should not affect the interannual dynamics. The time window applied for the SMOS latitudinal correction is [2013-2021] in order to reduce RFI contamination effect in the North hemisphere (see [AD12]).
- The different corrections are relative. As a result, SSS anomalies are available at the end of the correction processing. These anomalies are then calibrated against an absolute reference. The derived bias should be a time-independent correction in order to maintain the temporal dynamics of the SSS. This correction is done by using ISAS quantiles over a time window over the [2010-2022] period, after sss_qc and isc_qc flags filtering. In some cases (e. g. high latitudes), coastal biases are not constant over time due to variations in ice edges. A specific processing shall be found in these areas and will be the subject of future studies.
- In the settings of the various processing parameters (time correlation length, a priori variability), either spatially smooth fields, or slowly-evolving time fluctuations, are estimated to reduce errors as much as possible. This is why the CCI+SSS L4 products are split into two sub-products: a monthly product and a weekly product.

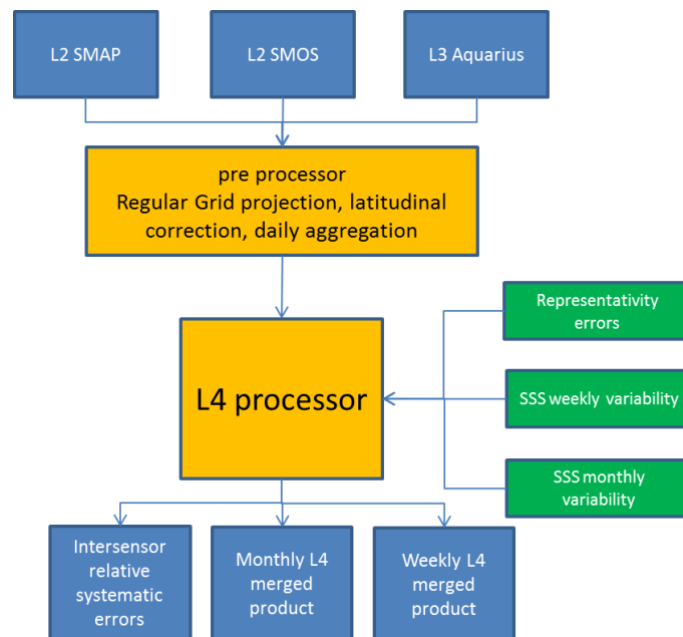


Figure 1: main L4 processing steps.

The algorithm steps to perform the corrections in order to estimate the unbiased SSS are as follows:

1. Correction of L2/L3 SSS from different biases. (see [AD12]).
2. Estimation of the inter-sensor biases and 30-day SSS are done simultaneously (section 2.2.2.4). The inter-sensor biases are considered constant for each month and evaluated assuming SSS varies slowly over a month (Figure 3). This computation is carried out by an optimal interpolation whose cost function is described in section 2.2.2.3.
3. Estimation of errors of the monthly SSS (section 2.2.2.7). Detection of outlier .
4. Correction of individual SSS and computation of a weekly-averaged SSS field (section 2.2.2.5). In this step, the bias correction is fixed and the 30-day SSS field is taken as a priori. We estimate fluctuations around this monthly field to achieve a time resolution of 7 days.
5. Estimation of errors of the weekly SSS (section 2.2.2.7).
6. Absolute calibration of SSS (section 2.2.2.6).

2.2.2 L4 algorithm

2.2.2.1 Generation of level 4 fields

To better understand the process, let's consider SSS_{obs} observations from a single sensor with a measurement covariance C_d . First, systematic uncertainties are ignored. To estimate an SSS time series of spatial resolution R_1 and temporal resolution T_1 , knowing that the observed data SSS_{obs} are at spatial resolution r_1 and temporal resolution t_1 , the cost function to be minimized is written (as a scalar product $\langle X|Y \rangle$):



$$C(SSS)=\langle SSS_{obs}-SSS | C_t^{-1} \cdot (SSS_{obs}-SSS) \rangle + \langle SSS-SSS_{prior} | C_2^{-1} \cdot (SSS-SSS_{prior}) \rangle \quad (1)$$

uncertainty C_r added to take into account the difference in resolution of fields $(R_1;T_1)$ and $(r_1;t_1)$:

$$C_t = C_d + C_r$$

This covariance is seasonal and specific to each grid node.

C_2 corresponds to the variability of the field with the spatio-resolution $(R_1;T_1)$ relative to the SSS_{prior} field. Again, this variability is seasonal and different for each grid node.

However, each sensor must be considered independently in the cost function considering the space and time resolution of each product. In the case where we estimate the monthly SSS field from the three sensors SMOS, SMAP, and Aquarius, we therefore have:

$$\begin{aligned} C(SSS) = & \langle SSS_{obs_smos}-SSS | C_{t_smos}^{-1} \cdot (SSS_{obs_smos}-SSS) \rangle + \\ & \langle SSS_{obs_smap}-SSS | C_{t_smap}^{-1} \cdot (SSS_{obs_smap}-SSS) \rangle + \\ & \langle SSS_{obs_aqua}-SSS | C_{t_aqua}^{-1} \cdot (SSS_{obs_aqua}-SSS) \rangle + \\ & \langle SSS-SSS_{prior} | C_2^{-1} \cdot (SSS-SSS_{prior}) \rangle \end{aligned}$$

In the SMOS Aquarius and SMAP covariance uncertainty, we add the representativity uncertainty that corresponds to the transition from acquisition time (about one second) to monthly resolution (30 days) or to weekly resolution (7 days). Also, covariance corresponding to variability is used in order to model the transition between monthly and weekly dynamic. These representativity uncertainties and this variability are computed from high resolution Mercator outputs.

Finally, the cost function also contains estimation of systematic uncertainty, also called biases. For each type of acquisition, a different relative bias is considered. Only a constant bias over the whole time series is taken into account, the latitudinal bias being corrected beforehand. An a posteriori uncertainty term, corresponding to a L4 SSS uncertainty, is also derived.

The methodology used to estimate observational random uncertainty, representativity uncertainty and SSS variability considered in the algorithm is described in the following sections. An example of climatological monthly SSS variability, the dominant term among the representativeness uncertainty and the variabilities between the several spatio-temporal scales involved in the OI, is illustrated on Figure 2. The main regions of high variability are consistent with expectations i.e. river outflow regions (Amazon, Congo, Mississippi, Ganges) and Gulf Stream variability.

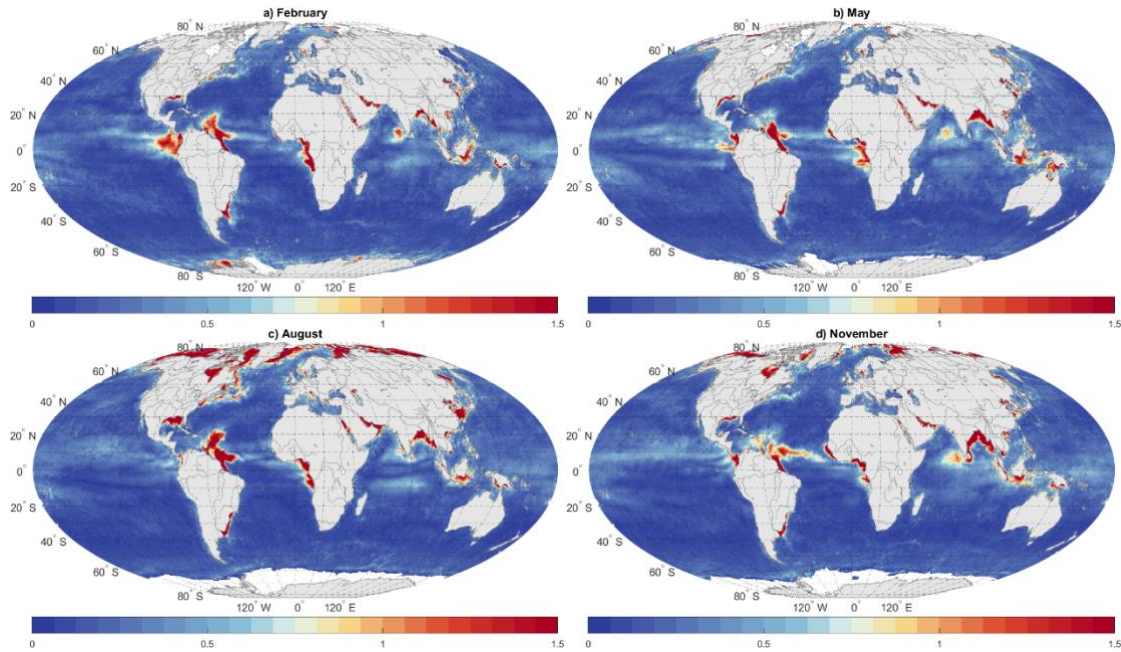


Figure 2: Examples of climatological maps of monthly SSS variability relative to the whole period SSS mean, that are considered in the optimal interpolation. a) February; b) May; c) August; d) November.

In order to estimate weekly SSS, we start from monthly SSS field estimate during the first step. In other words, the fluctuations of the weekly SSS are computed according to the monthly solution. For doing this in an OI context, we have to consider the variability of the weekly fluctuations relatively to the monthly field, i.e., not to consider the whole variability but only the relative variability. This variability has been computed by using Mercator field.

2.2.2.2 Systematic uncertainty of satellite SSS measurements:

We then remove main remaining systematic uncertainty following the methodology described in (Boutin et al., 2018) but applied to different sensors. It considers zonal seasonal varying biases (e.g. those linked to solar or galactic effects), as well as a constant bias over time which varies as a function of the location on the globe, the instrument and the geometry of observation (e.g. land-sea contamination):

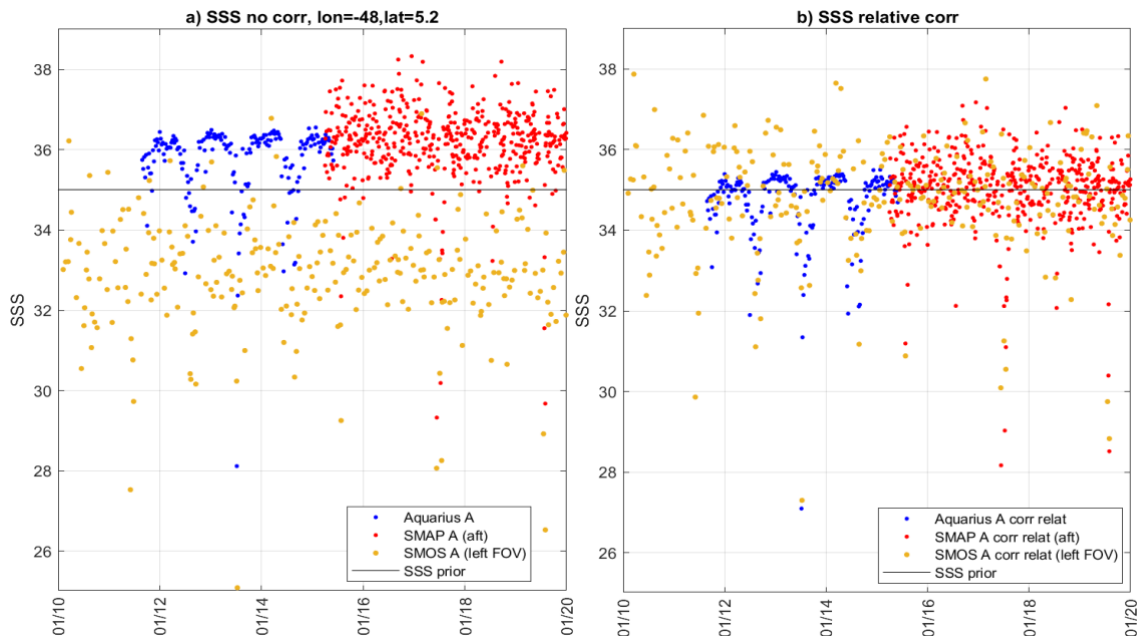
$$SSS_{obs}(t, \phi, \lambda, X, x_{orb}) = SSS_{ref}(\phi, \lambda) + SSS_{rel}(t, \phi, \lambda) - b_c(\phi, \lambda, X, x_{orb}) - b_{lat}(\phi, X, x_{orb}, m) \quad (1)$$

where SSS_{obs} is the observed SSS, t is the time of the measurement, ϕ , and λ are respectively the latitude and the longitude of the considered pixel over the ocean, X corresponds to a geometry of observation, x_{orb} indicating the satellite orbit direction (ascending or descending); b_c is a correction constant in time, b_{lat} is a zonal correction that varies seasonally as a function of the month, m . b_{lat} and b_c are relative corrections with respect to an arbitrary reference SSS constant over time, SSS_{ref} which corresponds to the prior SSS in the Bayesian scheme (see 2.2.2.3). The residuals of $SSS_{obs} - SSS_{ref} + b_c + b_{lat}$ correspond to the relative variations of SSS with respect to SSS_{ref} and are called SSS_{rel} (see example on Figure 3ab).

b_{lat} is pre-processed at L2/L3 sensor by sensor (see [AD12]) before b_c and SSS_{rel} retrieval.

b_c are derived with SSS_{rel} through a least square minimization approach, and through a series of iterations. The arbitrary reference SSS_{ref} is taken as the mean of ISAS SSS over 12 year period. At the end of the correction process, the whole corrected SSS time series are adjusted with a time-invariant shift derived from intercomparison of a quantile of corrected SSS and of ISAS SSS (Figure 3d). In regions with low SSS variability the 50% quantile (median) is considered, and it is increased up to 80% in regions with high SSS variability, where SSS statistical distribution is skewed towards low values which are not well represented in ISAS fields, due to the Argo undersampling and ISAS smoothing.

At L-Band (frequency of 1.4GHz), the penetration depth (the skin depth) is 1cm. In most situation, this depth represents well the first meters of the upper ocean, except for a few hours after a rainfall or in very stratified regions like river plumes. In rainy areas, the SSS retrieved from L-Band radiometers is fresher than the ones measured at a few meters' depths or in the non-rainy surrounding regions. On monthly SSS averaged over a longitudinal band centred on the ITCZ this effect is estimated to be up to 0.1, smaller in other regions [32]. Hence, before merging products, the salinity freshening associated with instantaneous rain rate has been corrected or filtered out in SMOS and SMAP salinities entering in CCI L4 v4 SSS using, for SMOS, a relationship between salinity freshening, wind speed and satellite rain rate (IMERG) [AD12].



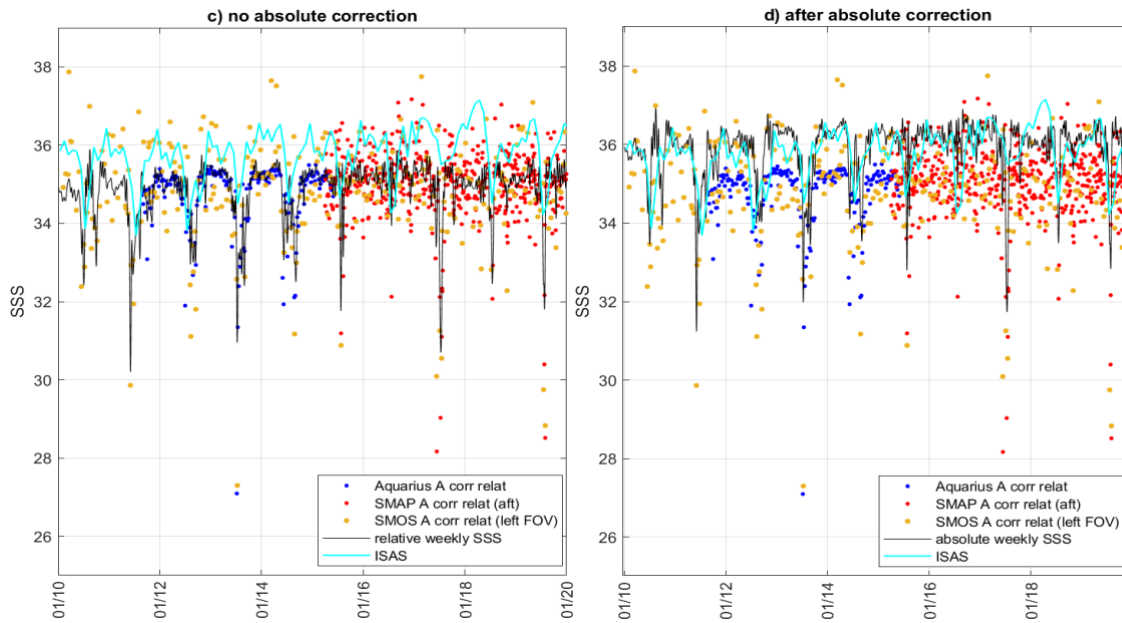


Figure 3: Principle of the self-consistency approach. Example of a grid point near the Amazon plume (48°W, 5.2°N) affected by land sea contamination, seen under various satellite geometry during ascending orbits (SMOS L2 SSS, left hand side of the FOV, green points; SMAP L2 SSS, aft antenna, red points; Aquarius L3 daily SSS, blue points). a) Satellite SSS before correction (SSS_{obs} and SSS_{ref} (black line) ; b) Satellite SSS after relative adjustment ($SSS_{rel}+SSS_{ref}$) and SSS_{ref} (black line); c) Satellite SSS after relative adjustment ($SSS_{rel}+SSS_{ref}$), weekly OI relative SSS (black) and ISAS SSS (light blue); d) Same as c) but after absolute calibration of the weekly OI SSS by adjusting the 80% quantile of the weekly OI SSS statistical distribution to that of the ISAS SSS.

2.2.2.3 Parameter estimation

The algorithm is therefore looking for solutions $SSS(t)$ and b_c that both minimizes the cost function. Each grid node is processed separately. All available SSS data associated with the grid node considered are used by the algorithm. The problem is linear. To minimize the cost function, a classic Raphson-Newton descent is used.

SSS_{obs} is the observation vector that contains SMOS, SMAP and Aquarius data:

$$SSS_{obs} = \begin{pmatrix} SSS_{smos} \\ SSS_{aqua} \\ SSS_{smap} \end{pmatrix}$$

The parameter vector is written:

$$m = \begin{pmatrix} SSS \\ bc_{smos} \\ bc_{aqua} \\ bc_{smap} \end{pmatrix}$$



bc_smos, bc_aqua, bc_smap are vectors that contain the biases for each type of acquisition (ascending/descending, dwell lines, fore-aft ...etc) that can be grouped into a vector bc. We will take as a priori bc=0 for all sensors and acquisition types. SSS is a function according to the time and is estimated every day over the 10 year period.

The vector parameter a priori is written:

$$m_{\text{prior}} = \begin{pmatrix} SSS_{\text{ref}} \\ 0 \\ 0 \\ 0 \end{pmatrix}$$

SSS_{ref} is the starting SSS used as a priori (this value is constant over time). It is taken equal to the mean ISAS SSS taken over 10 years.

If we call H, the matrix of partial derivatives:

$$H = \begin{bmatrix} \frac{\partial SSS_{\text{smos}}}{\partial SSS} & \frac{\partial SSS_{\text{smos}}}{\partial bc_{\text{smos}}} & \frac{\partial SSS_{\text{smos}}}{\partial bc_{\text{aqua}}} & \frac{\partial SSS_{\text{smos}}}{\partial bc_{\text{smap}}} \\ \frac{\partial SSS_{\text{aqua}}}{\partial SSS} & \frac{\partial SSS_{\text{aqua}}}{\partial bc_{\text{smos}}} & \frac{\partial SSS_{\text{aqua}}}{\partial bc_{\text{aqua}}} & \frac{\partial SSS_{\text{aqua}}}{\partial bc_{\text{smap}}} \\ \frac{\partial SSS_{\text{smap}}}{\partial SSS} & \frac{\partial SSS_{\text{smap}}}{\partial bc_{\text{smos}}} & \frac{\partial SSS_{\text{smap}}}{\partial bc_{\text{aqua}}} & \frac{\partial SSS_{\text{smap}}}{\partial bc_{\text{smap}}} \end{bmatrix}$$

where

$$SSS_{\text{sensor}} = F(m) = SSS - bc_{\text{sensor}}$$

with "sensor" = smos (SMOS), aqua (Aquarius) or smap (SMAP).

This matrix is calculated on the observation points.

The covariance matrices used are as follows:

- Cd the error matrix,
- Cm the matrix of SSS variability and a priori error on bc,
- Cr the matrix of representativity errors.

$$C_d = \begin{bmatrix} C_{d_smos} & 0 & 0 \\ 0 & C_{d_aqua} & 0 \\ 0 & 0 & C_{d_smap} \end{bmatrix}$$

$$C_m = \begin{bmatrix} C_{SSS} & 0 \\ 0 & C_{bc} \end{bmatrix}$$



CSSS is a time smoothing operator that contains the expected variability that is provided as auxiliary data. Thus, the covariance of the SSS that links two times t1 and t2 is written:

$$CSSS(t1,t2)=sigSSS(t1)sigSSS(t2)\exp\left(-\frac{(t1-t2)^2}{\xi^2}\right)$$

with $\xi=25$ days and 6 days for monthly and weekly products respectively.

"sigSSS" is interpolated temporally to the acquisition times from seasonal variability.

"Cbc" is a diagonal matrix that contains the a priori standard deviation of biases. This standard deviation is set at 4pss.

The Cr matrix corresponds to representativity errors:

$$Cr = \begin{bmatrix} Cr_smos & 0 & 0 \\ 0 & Cr_aqua & 0 \\ 0 & 0 & Cr_smap \end{bmatrix}$$

In addition to measurement errors, representativity errors are added:

$$Ct=Cd+Cr$$

Representativity errors are reported monthly. They are interpolated temporally to the acquisition times.

In this formalism, the cost function is written, for each grid node:

$$C(SSS, bc) = \langle SSS_{obs} - F(m) | Ct^{-1} \cdot (SSS_{obs} - F(m)) \rangle + \langle m - m_{prior} | Cm^{-1} \cdot (m - m_{prior}) \rangle$$

with:

$$F(m) = SSS - bc$$

We look for SSS_est and bc_est that minimize C(SSS, bc). The solution of minimization is written:

$$m_est = m_prior + Cm \cdot H^T \cdot (H \cdot Cm \cdot H^T + Ct)^{-1} \cdot (SSS_{obs} - F(m_prior))$$

where "T" indicates the transpose operator.

2.2.2.4 Estimation of monthly SSS

In order to estimate the monthly SSS, we proceed in 3 steps:



- 1) a first estimation of the biases and time series of SSS, grid node by grid node is performed,
- 2) a 3-sigma filtering of the observed SSS in comparison with the estimated SSS is done.

The aim here is to identify any outliers against the returned SSS field. Outliers can be linked to intermittent RFIs. It is considered here that stable RFI contamination can be corrected.

- 3) a second estimate of SSS biases (b_c) and SSS time series after removing outliers.

The relative biases b_c are estimated from the averaged ISAS SSS taken as SSS a priori.

2.2.2.5 Estimation of weekly SSS

To estimate the weekly SSS, the biases calculated at the monthly SSS are frozen (it is assumed that the biases will not be better estimated from a weekly smoothing). We start from the monthly SSS as a priori. We try to estimate the weekly fluctuations around this a priori. We estimate the weekly fluctuations around this a priori, taking into account the acceptable SSS variability between weekly and monthly fields that was derived as a monthly climatology from the Mercator model. A 3-sigma filter is used in order to eliminate outliers that deviate too far from what is expected. Here, $\sigma = \sqrt{\text{error_L2}^2 + \text{variability}^2}$. This eliminates outliers that deviate too far from what is expected. The weekly SSS field estimate is done in a single step.

2.2.2.6 Absolute correction

At the end of the inter-sensor bias correction step, the salinities obtained are set on average of the SSS of all sensors. However, the SSS estimation can itself be affected by a bias. This is corrected by adjusting a quantile of the CCI and ISAS SSS statistical distributions in each grid node over the period considered. The dynamics of the SSS are not affected by this adjustment as only one constant value, grid node per grid node, is added for the entire period. In regions where SSS variability is low, we assume that high frequency variability better sampled by CCI than by ISAS does not affect significantly the median of the SSS and we therefore adjust both SSS median (50% quantile). In regions with larger variability, given that intermittent freshening is much more frequent than intermittent over-salting, we expect the high part of the SSS distribution to be less affected by the higher frequency sampling by satellite than by ISAS. Hence in case of high weekly variability, we perform the calibration of CCI SSS on ISAS SSS, not by using the median but a high quantile, in order to promote the calibration on the high SSS values. A high quantile is not used everywhere as in case the SSS error is greater than the variability, the high quantile of the satellite SSS is expected to differ (be higher) from the one of ISAS.

If the variability is greater than 0.8, the quantile is taken as 80%. If the variability is between 0.6 and 0.8, we take a quantile intermediate between 50% and 80% that varies linearly with the SSS variability. The map of quantiles used for the absolute calibration of the SSS is given in Figure 4.

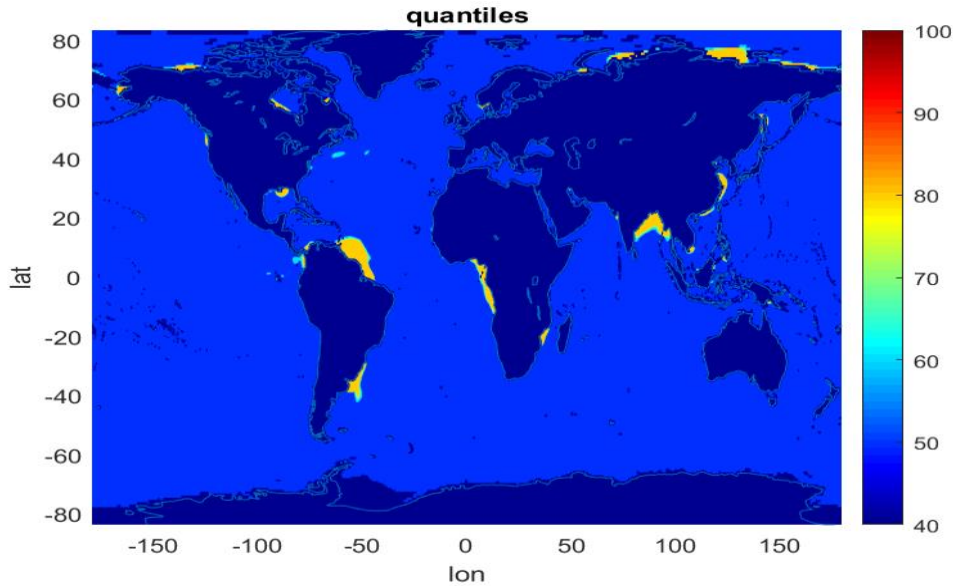


Figure 4: Quantile map used for the SSS absolute calibration. x and y axis units in pixel number for longitude and latitude respectively.

2.2.2.7 Error budget

The computation of theoretical errors is obtained directly from the pseudo hessian matrix.

$$C_{post} = C_m - C_m \cdot H^T \cdot (H \cdot C_m \cdot H^T + C_t)^{-1} \cdot H \cdot C_m$$

Note that the error *a posteriori* is necessarily lower than the variability introduced via the operator C_m . In the monthly case, this variability corresponds to the expected monthly fluctuations shown in Figure 2. In the weekly case, the variability is calculated relative to the monthly field. The latter is generally lower than the monthly variability. The *a posteriori* error obtained on the weekly fields should therefore be lower than that obtained on the monthly fields. However, this is only true if, to obtain the weekly fields, we started from noise-corrected monthly fields, which is not the case. The propagation of errors on the weekly fields must therefore take into account errors on the monthly field. Thus, for the monthly fields, we have:

$$C_{post_month} = C_{m_month} - C_{m_month} \cdot H^T \cdot (H \cdot C_{m_month} \cdot H^T + C_t)^{-1} \cdot H \cdot C_{m_month}$$

and for the weekly fields:

$$C_{post_week} = C_{m_tot} - C_{m_tot} \cdot H^T \cdot (H \cdot C_{m_tot} \cdot H^T + C_t)^{-1} \cdot H \cdot C_{m_tot}$$

where :

$$C_{m_tot} = C_{m_month} + C_{m_week}$$

with C_{m_month} , the monthly variability and C_{m_week} , the weekly variability relative to the monthly variability.



The a posterior errors on the monthly and weekly fields are therefore obtained as follows:

$$\sigma_{SSS_{\text{month}}} = \sqrt{\text{diag}(C_{\text{post_month}})}$$

$$\sigma_{SSS_{\text{week}}} = \sqrt{\text{diag}(C_{\text{post_week}})}$$

The number of outliers is also calculated on this same basis as well as the number of data available. The window sizes used are respectively +/- 30 days and +/- 10 days for monthly and weekly products respectively.

In order to give an idea of the impact of the data in terms of information, a specific indicator named PCTVAR is computed. It corresponds to the ratio of the a posteriori variance (the square of the a posteriori error) with the a priori variance. This gives the part of the variability which is unexplained by the data. This ratio belongs to the interval [0 100] (if expressed in %) and larger value shows low contribution of SSSobs (because of too large measurement errors in comparison with the expected variability).

2.2.2.8 Flags

Three quality flags are computed : a global quality flag, a sea-ice flag and a coastal flag.

Ice flag (isc_qc)

Acard averaged over a 10 days slipping window gives a good indicator of ice contamination. This time average is done independently for each grid point.

For each grid point and each time step, the ice flag is raised (only on zones 45N-85N and 45S-85S) if the following conditions are met:

- the averaged Acard over the time window (+/- 5 days) is less than 40.
- the SST is lower than 8°C

An intermediate averaged Acard product is generated offline by using SMOS L2 products.

Coastal mask and land-sea flag (lsc_qc)

The coastal mask has been revised in order to retrieve SSS as close as possible to the land (up to less than 50km from the coast) and in order to ignore the small islands. The risk of contamination by land is therefore very high. This is why we are proposing a conservative strategy for flagging land-sea contamination which corresponds to the one used in CATDS..



Quality flag (sss_qc)

The quality flag is calculated on a criterion of the number of outliers. The number of outliers is calculated over a window of +/- 30 days for monthly salinities and over a window of +/- 10 days for weekly salinities. It corresponds to the number of SSSobs which deviates by more than 3 sigmas from the estimated SSS. If the fraction of outliers is larger than 10%, the flag is raised.



3 Conclusions and way forward for L-band sensor Algorithm

SSS measurements from the three L-band satellite sensors have been merged to produce CCI L4 SSS time series over a decade at global scale. The methodology we have developed for building the CCI L4 dataset aims at preserving the SSS variability globally observed by satellite every few days in footprints integrated over typically 50 x 50 km². No spatial smoothing nor temporal relaxation to in-situ SSS have been introduced in order to keep as much as possible SSS interannual variability sensed by original SSS satellite measurements. On another hand, the self-consistency between satellite SSS measured by the various sensors and under various geometries have been used to correct for systematic uncertainties. External SSS information is considered only for calibrating the long term SSS absolute value and for estimating representativity uncertainties. The CCI+SSS approach is, therefore, upstream of the optimal interpolations which correct satellite SSS biases using in-situ SSS fields on a monthly basis or less, such as (Melnichenko et al., 2016), and the CCI+SSS fields could be used as inputs to such method, as was done with SMOS data (Nardelli et al., 2016) or with SMOS and SMAP data (Kolodziejczyk et al., 2020).

Nevertheless, some issues have been identified in the PVASR which remain to be tackled in future versions:

- in the high northern latitudes, both seasonal latitudinal biases and land-sea contamination (and/or ice-sea) contamination affect all SMOS ocean pixels. Hence a method which separates the determination of the two (or three) types of contamination does not allow to remove all the contaminations. The methodology should be adapted to deal with both contaminations.
- it remains interannual variation of SMOS SSS biases after systematic bias correction. A specific L2OS processing will be implemented for CCI SSS v5 products by using ERA5 and an update of the PCA algorithm allowing to remove intermittent biases. Some tests will be done in order to look at the possibility to remove ice edge effect from PCA algorithm.. PCA method will be generalized over more RFI sources (see [AD12]).

4 AMSR-E C- and X-band SSS retrieval Algorithm

4.1 SSS retrieval Algorithm Overview

4.1.1 Historical Background and general approach

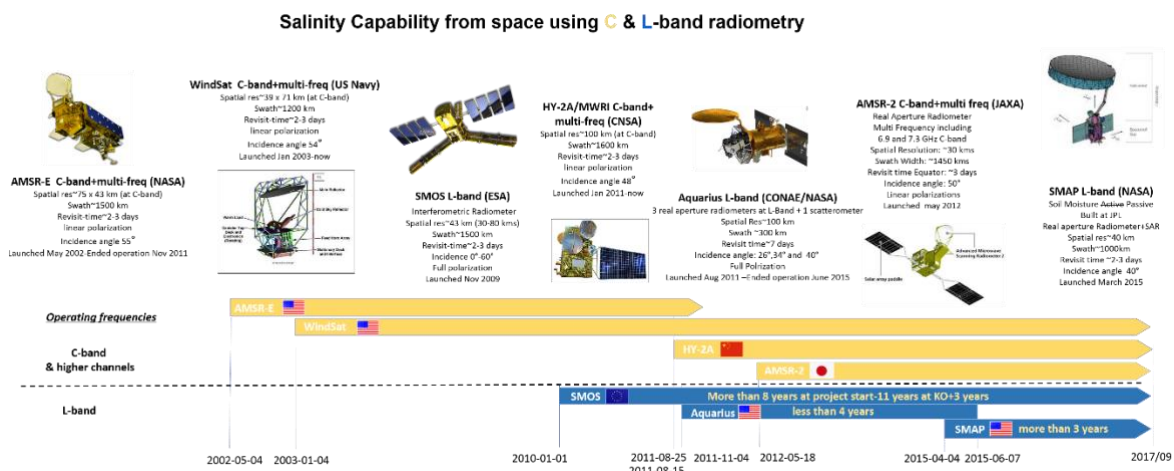


Figure 5: Sketch showing the different satellites operating low-microwave frequency radiometers characteristics from which SSS remote sensing from Space can be estimated in the modern satellite era. Along the timeline, C-band sensors are shown in orange while L-band ones are in blue.

The potential SSS retrieval capability from low frequency spaceborne radiometer data operated at C- (6.9 GHz) and X- (10.7 GHz) band beyond several other higher microwave frequencies (AMSR-E, AMSR-2, WindSAT, or, HY-2A, see Figure 5) has been demonstrated in RD01 for the very high SSS gradients and warm Amazon river Plume area. This principle was more recently applied to the SSS signal in the China Sea (RD02) using the same frequency channels data from the microwave radiometer onboard the HY-2A satellite.

As illustrated in Figure 1, the main SSS-satellite era is covering the period 2010-now when L-band observations started with SMOS mission. C-band data can however also be used to cover some regional specificities of the SSS fields back in time to 2002. Combining C/X-band historical data with the L-band era, this would allow the generation of almost 20-years long satellite SSS time series in some key regional area for the water cycle. In the frame of this project, we started by only considering the C/X-band SSS data from AMSR-E radiometer. WindSAT data are not considered at the beginning of phase-2 as the radiometer calibrated L1 data were not yet publicly available. They are now partially available at <https://cmr.earthdata.nasa.gov/virtual-directory/collections/C2559430954-POCLOUD/temporal> for several years (2015,2016,2017) and will be considered for the next phases of the project.. By virtue of signal sensitivity, SSS retrievals (Reul et al., 2009) from differential C- and X-bands channel data combined with multi-higher frequency channel ones (e.g., AMSR-E) are limited to region exhibiting very high SSS gradients

(>4-5 ps) and apply in warm seas for which the sensitivity is highest (e.g. tropical river plumes). We developed AMSR-E based SSS products for four specific river plume dominated warm oceanic regions to monitor strong frontal zones and over an extended time period back to 2002 with respect the L-band era. The selected regions (see Figure 6) include:

-Region 1: The Amazon and Orinoco River Plume region, which is analysed within the following spatial domain (hereafter referred to as the AORP domain): [5°S-30°N; 80°W-25°W]

-Region 2: The Congo and Niger River plumes, which is analysed within the following spatial domain (hereafter referred to as the CNRP domain): [20°S-10°N; 10°W-20°E]

-Region 3: The Mississippi river plume (MRP) region, which will be analysed within the following spatial domain (hereafter referred to as the MRP domain): [18°N-30°N; 100°W-80°W]

-Region 4: The Ganges, Brahmaputra, Irrawady river discharges, which will be analysed within the following spatial domain (hereafter referred to as the BoB domain): [5°S-25°N; 75°E-110°E]

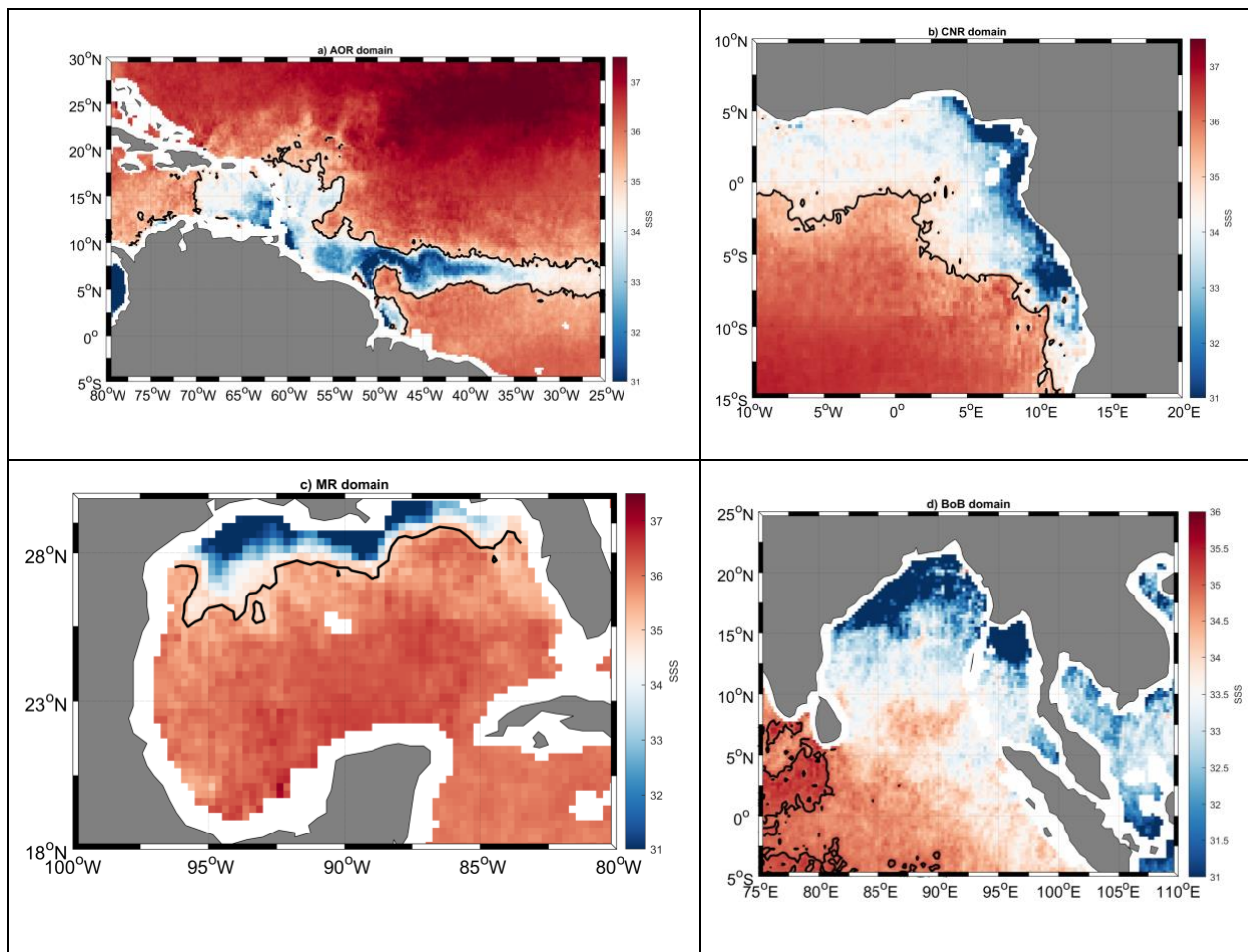


Figure 6: Spatial Domain of the regional AMSR-E based SSS products developed for the CCI project

Though the response of sea surface reflectance/emissivity to surface salinity is significantly weaker in the C- and X- bands compared with L-band used on the SMOS, Aquarius-SAC/D or SMAP

satellite missions (see Figure 7), the relative sensitivity of the signal to SSS with respect wind and SST is nonetheless significantly improved after differentiating the estimated sea surface reflectance frequential contrast between the C- and X –bands. We explain this further below.

The major objective of the AMSR, AMSR-E, AMSR-2, WindSat or HY-2A microwave radiometers is to acquire global observations of the sea surface temperature, wind speed, water vapor and cloud liquid water. These instruments are (in general) equipped with twelve channel, six-frequency, passive microwave radiometer system. They measure horizontally and vertically polarized brightness temperatures at 6.9 GHz, 10.7 GHz, 18.7 GHz, 23.8 GHz, 36.5 GHz, and 89.0 GHz and with incidence angle $\sim 53-55^\circ$. Note that AMSR-2 has 2 additional frequency channels at 7.3 GHz used for RFI detection. In this first version of the C/X band-based CCI SSS products we shall only consider AMSR-E based SSS products as this sensor can provide SSS time series back to 2002.

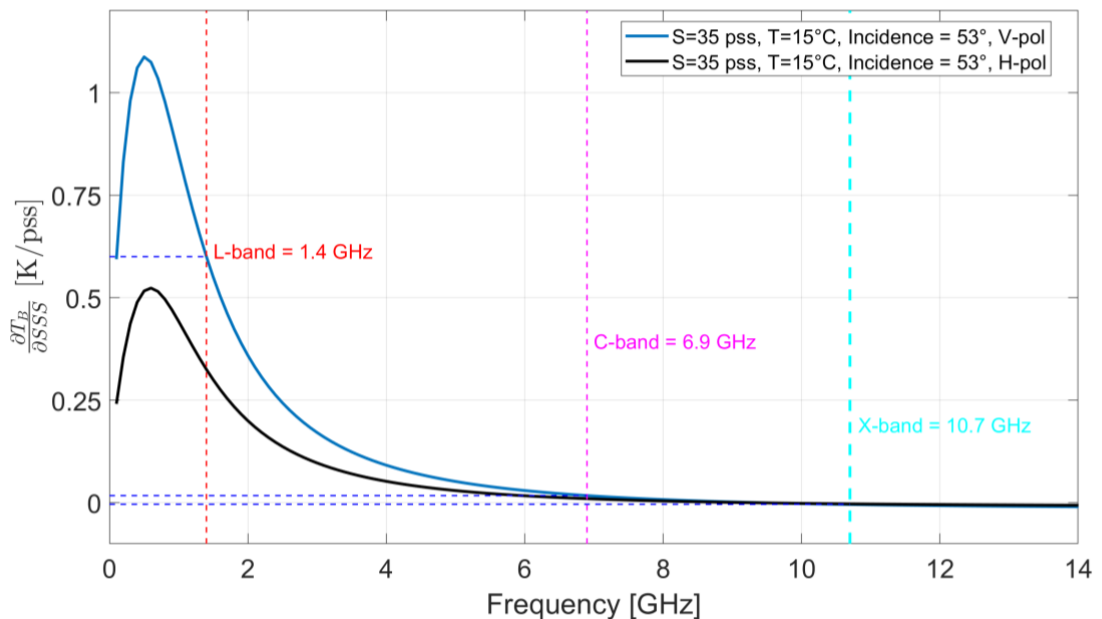


Figure 7 Sensitivity of the flat ocean brightness temperature to SSS, namely, $\frac{\partial T_B}{\partial SSS}$ as a function of electromagnetic frequency (x-axis) computed from Klein and Swift (1977) for the salinity of 35 psu and temperature of 15°C with a fixed incident angle of 53°.

As shown in Figure 7, the response of the sea surface reflectance to sea surface salinity is sensitive near 1.4 GHz and drops sharply as microwave frequency increases for a given SST for both horizontal and vertical polarizations (H-pol and V-pol), while the signal is stronger for the V-pol. At 53° of incidence, SST=15°, SSS=35 psu, and V-polarization, the sensitivity thus drops from ~ 0.6 K/psu at L-band to ~ 0.04 K/psu at C-band and the brightness is almost insensitive to SSS at X-band. L-band is therefore much more sensitive to SSS than is C-band and this is even more the case for X-band. Retrieving SSS from C-band sensor is therefore very challenging and demands extremely accurate algorithms.

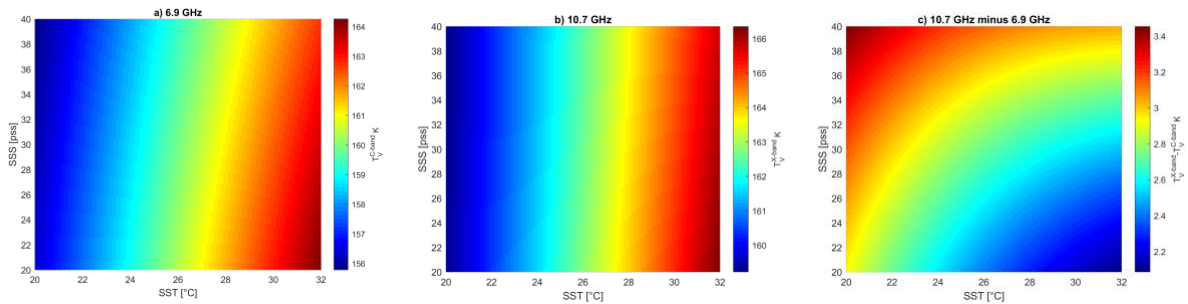


Figure 8 Brightness temperature of the flat sea surface in microwave bands as functions of SSS (y-axis) and SST(x-axis). (a) brightness at 6.9 GHz (C band) (b) Brightness at 10.7 GHz (X band) in V-pol and (C) brightness temperature difference between the 10.7 GHz and 6.6 GHz in V-pol.

To evidence nonetheless the capability of C/X band radiometer channels for measuring the sea surface salinity, the brightness temperature of the sea surface in microwave bands is computed as functions of SSS and SST (Figure 8) following Meissner and Wentz [2004]’s model for the dielectric constant of sea water. At low frequencies, this model is a modified version of the Klein–Swift’s 1977 model (see details in section 2).

For a given SST, the flat ocean surface T_b in V-polarisation decreases monotonically with increasing SSS, while the reflectance of sea surface increases due to the presence of saline materials that increase the dielectric properties of sea water and thus decrease the emissivity or increase the reflectance. Meanwhile, for a given SSS, the surface emissivity (reflectance) increases (decreases) due to higher molecular energy with higher temperature (Figure 8 a & b). By differentiating the reflectance between the C and X band in vertical polarisation, it is clearly seen in Figure 8c and Figure 9 that both SSS and SST have apparent impacts on the differential sea surface reflectance contrast between X- and C-bands, which is defined as:

$$\text{or } \Delta T = T_{10.7V} - T_{6.9V} \text{ or } \Delta R = R_{6.9V} - R_{10.7V}$$

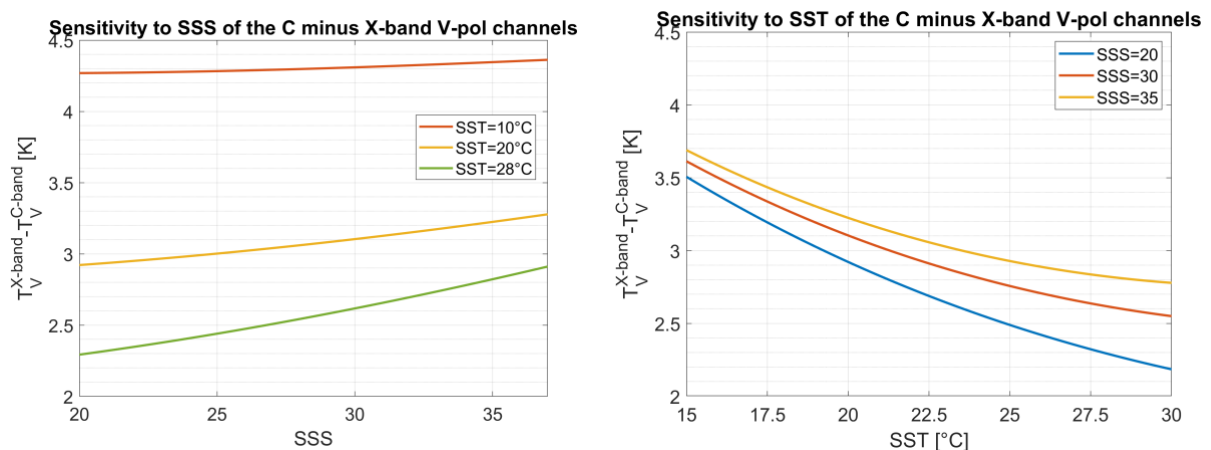


Figure 9: Change of the differential flat ocean surface brightness temperature with SSS for fixed values of SST (left) and with SST for fixed values of SSS (right).

At an SST of 28°C (see Figure 9), a change of 10 psu in salinity from 25 to 35 psu corresponds to a change of flat sea surface brightness temperature contrast ΔT of ~ 0.4 K. Comparatively, at an



SSS=35 (typical of open ocean conditions), a change of 10°C in SST induces also a change of $\Delta T \sim 0.4$ K. Therefore, in the warm tropical oceans, the sensibility to SSS of the quantity ΔT ($\sim 0.04\text{K/pss}$) is comparable to its sensitivity to SST ($\sim 0.04\text{K/}^\circ\text{C}$).

Given an auxiliary information on the SST, SSS can thus be derived from ΔT using the model shown in Figure 8c or using an empirically-derived model of this function. An accurate estimation of the ‘flat’ surface brightness frequency-differential contrast ΔT or ΔR quantity is therefore a key step of the proposed algorithm.

4.1.2 AMSR-E sensor and characteristics

The Advanced Microwave Scanning Radiometer for EOS (AMSR-E) is a twelve-channel, six-frequency, total power passive-microwave radiometer system. It measures brightness temperatures at 6.925, 10.65, 18.7, 23.8, 36.5, and 89.0 GHz. Vertically and horizontally polarized measurements are taken at all channels. The Earth-emitted microwave radiation is collected by an offset parabolic reflector 1.6 meters in diameter that scans across the Earth along an imaginary conical surface, maintaining a constant Earth incidence angle of 55° and providing a swath width array of six feedhorns which then carry the radiation to radiometers for measurement. Calibration is accomplished with observations of cosmic background radiation and an on-board warm target. Spatial resolution of the individual measurements varies from 5.4 km at 89.0 GHz to 56 km at 6.9 GHz. The dates of operation of AMSR-E are May 2002 to Oct 2011.

Table 2 Aqua/AMSR-E Instrument characteristics compared to L-band satellite radiometers

Instrument	Frequency (GHz)	Spatial resolution [km x km] (3-dB footprint size)	Earth Incidence angle (°)	Ne ΔT^* (K)	Polarizations	Swath Width (km)
SMAP	1.4 L-band	39 x 47 km	40°	0.9	H, V, 3rd & 4th Stokes	~1000 km
SMOS	1.4 L-band	30-60 km	0°-60°	1-2 K	H, V, 3rd & 4th Stokes	~1200 km
Aquarius	1.4 L-band	76 km x 94 km 84x120 km 95x156 km	28.7°, 37.8° 45.6°	0.2	H, V, 3rd & 4th Stokes	~300 km



AMSR-E	6.93 C-band		75 x 43 km =Res 1	55	0.3	V,H	~1450km.
	10.65 X-band		51 x 29 km =Res2	55	0.6	V,H	
	18.7 band	K-	27 x 16 km =Res3	55	0.6	V,H	
	23.8 band	K-	32 x 18 km =Res4	55	0.6	V,H	
	36.5 band	Ka-	14 x 8 km =Res5	55	0.6	V,H	
	89.0 band	W-	6 x 4 km =Res6	55	1.1	V,H	

AMSR-E observes the Earth at 6.9, 10.7, 18.7, 36.5, and 89 GHz, where each frequency has a native footprint size associated with it. The AMSR-E Level-2A (L2A) product from the National Snow and Ice Data Center (NSIDC) contains a set of spatially coherent data sets corresponding to each of these native footprint sizes. This data set complement and extend NSIDC's existing EASE-Grid brightness temperature data sets, with new data beginning June 2002 and continuing throughout the life-cycle of the instrument.

AMSR-E L2A data contain data for each observed frequency in all resolutions equal to or higher-valued (larger field of view) than its native one. That is, all channels are available in their own native footprint, as well as any larger footprint. When 10 GHz data is selected with resolution 1, the resulting effective footprint matches that of the 6 GHz native footprint. This is useful as we are deriving algorithms and producing products that involve more than one frequency. As a general rule, the resolution of all channels for algorithm development should share a common footprint size. While some information is lost by doing this, the benefit of consistent antenna observations is gained. We have chosen the L2A data resolution that we believe to be most suitable, i.e, the C-band resolution (Res 1) which is about 58 km in average.



The SST algorithm uses all 10 AMSR-E lower channels, while the wind algorithm does not use the 6.9 GHz channels. The reason is that 6.9 GHz is not significantly improving the wind retrievals and hence by not using it, one can obtain wind retrievals at a higher spatial resolution.

The columnar water vapor and columnar liquid cloud water algorithms also have a similar structure. These two algorithms only use the 19, 23, and 37 GHz channels.

The radiometer noise figure for one 6.9 GHz observation is 0.3 K. However, the 6.9 GHz observations are greatly over sampled. Observations are taken every 10 km, but the spatial resolution of the footprint is 58 km. During the Level-2A processing, adjacent observations are averaged together in such a way as to reduce the noise to 0.1 K. In doing this averaging, the spatial resolution is degraded by only 2%.

Note that in contrast to IR retrieval techniques, the atmospheric interference at 6.9 GHz is very small and easily removed using the higher frequency channels, except when there is rain. And, observations affected by rain are easily detected and can be discarded. Thus, the atmosphere does not pose a problem for the SST retrieval. An SSS climatology (WOA) is used to correct for mean SSS impact on the REMSS SST retrieval. This is one reason why we first used an independent auxiliary SST product (CCI-SST from IR data) for the SSS retrieval from AMSR-E. The CCI-SST However, we found that there are large differences between ascending and descending passes, some of which could be attributed to the diurnal SST cycles. AMSR-E ascending and descending tracks are 12 hours apart, with the satellite ascending passes at ~01:30 pm and descending passes at ~01:30 am (local time), implying that there can be significant differences in the SST. We found that the REMSS AMSR-E SST exhibit significant diurnal cycle in the 4 regions considered (with differences reaching about 2°C, which is the equivalent of 2 pss between day and nighttime), varying seasonally and geographically. During the present algorithm development, we first used the CCI Infrared based daily composite GHRSSST SST products as the auxiliary SST data. Although independent from AMSR-E SST data, the later is a night-time foundation SST estimate. However, neglecting the strength of the diurnal SST cycle induced large errors on the retrieved SSS and we therefore now use the local, both in space and time, AMSR-E SST data for the present algorithm.

While the AMSR-E RTM algorithm was tuned for SST and wind speed retrieval, much more precise atmospheric corrections are needed in the case of SSS retrievals. For these reason, we first correct the AMSR-E antenna Tb at 6.9 GHz and 10.7 GHz for atmospheric effects using the RTM model developed by Wentz and Meissner and Wentz for SST and wind retrieval but we have additional empirical adjustments to refine the model.

4.1.3 Algorithm Overview

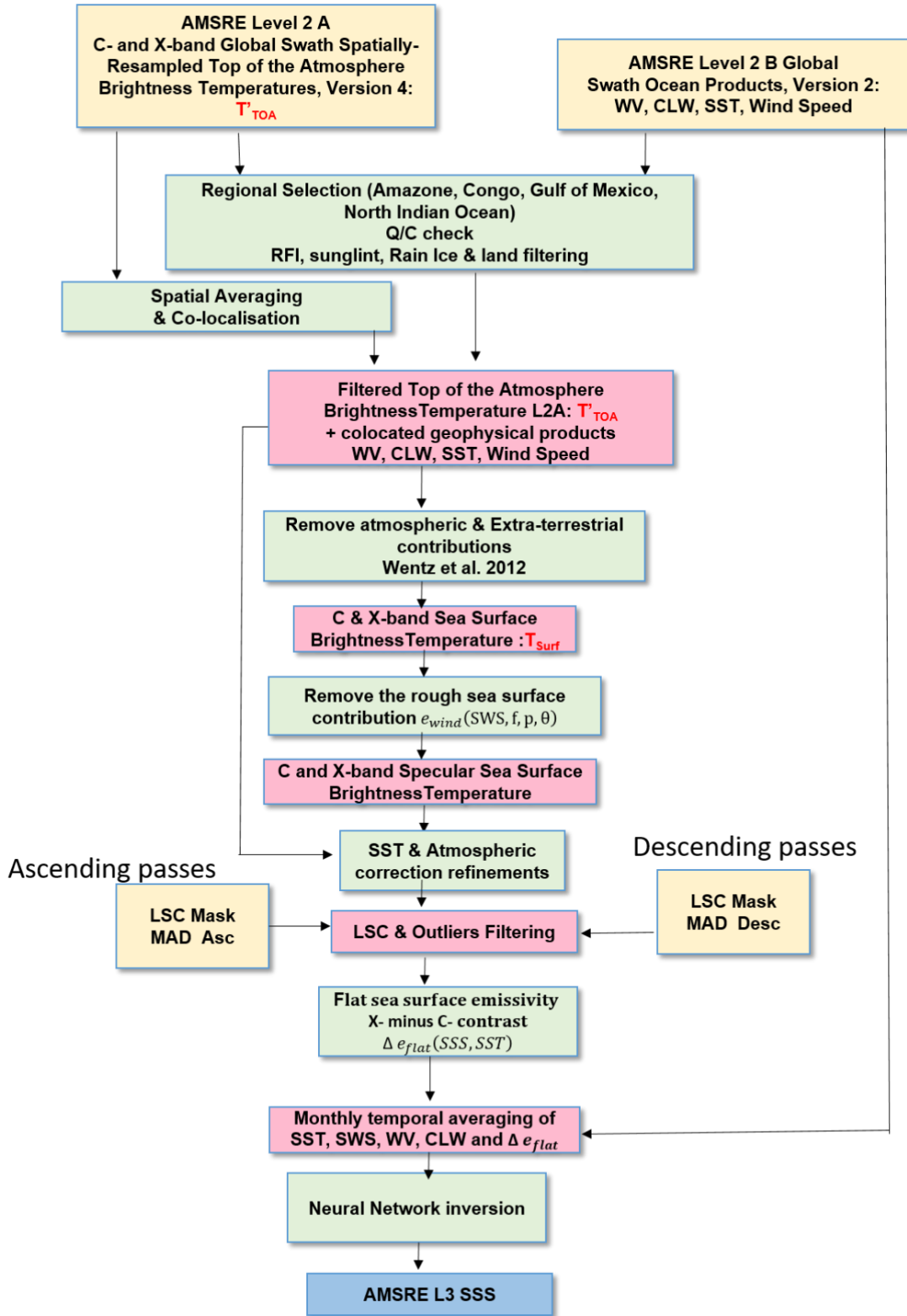


Figure 10: Sketch showing the flow of the AMSR-E SSS retrieval



A sketch of the Algorithm is shown in Figure 10. The major steps of the algorithm are reviewed hereafter.

4.1.3.1 Step 1: Input Data collection

A common database of input AMSR-E L2A T_B and L2B ocean products (organized as daily 50 minute half-orbit swath) are collected daily (see section 4.2 for details) over the four specific regions of warm oceanic regions with high SSS gradients:

- Region AORP: Amazon & Orinoco river plumes [80°W-25°W;5°N-30°N]
- Region MRP; Mississippi river plume [100°W- 80°W;18°N-30°N]
- Region CNRP: Congo Niger river plume: [10°-20°E; 20°S- 10°N]
- Region BoB: Bay of Bengal [75°E-110°E;5°S- 25°N]

4.1.3.2 Step 2: Input Data Quality Control

Surface types and brightness temperatures are examined for land, sea ice, and other sources of contamination (Radio Frequency Interference, Sun glint, rain, etc..). Ocean variables are not calculated for these areas. For all variables, values that are out of range are not included. Instead, the resulting product pixel indicates an out-of-range condition.

4.1.3.3 Step 3: Data re-gridding

The AMSR-E L2A & L2B products, which are including the antenna brightness temperature in Vertical Polarization at 6.9 GHz, namely, $T_{A;6.9}^V$, and at 10.7 GHz, $T_{A;10.7}^V$, as well as the AMSR-E surface wind (U_{10}), sea surface temperature (SST), columnar cloud liquid water (CLW) and the columnar Water vapor (WV) are spatially averaged at AMSR-E resolution (56 km) and re-gridded on a $\frac{1}{4}^\circ \times \frac{1}{4}^\circ$ rectangular grid.

4.1.3.4 Step 4: From Antenna to Specular ocean Surface brightness

The SSS retrieval algorithm is based on the physical Radiative Transfer Model (RTM) described in (Wentz and Meissner 2000). The RTM consists of an atmospheric absorption model for water vapor, oxygen, liquid cloud water, and a sea surface emissivity model that parameterizes the emissivity as a function of sea surface temperature, sea surface salinity and sea surface wind speed. Extra-terrestrial contributions (solar, Microwave background) and their reflection are corrected for. Then, atmospheric effects (direct and sea surface scattered) are removed from the antenna signal using the SST and the AMSR-E retrieved wind (U_{10}), columnar cloud liquid water (CLW) and the columnar Water vapor (WV). Some components of the model were updated in recent versions of the algorithm including the dielectric constant of sea and cloud water (Meissner and Wentz 2004; 2006). This was taken into account.



At the end of this processing step, we obtain estimates of the sea surface brightness temperature in Vertical Polarization at 6.9 GHz, namely, $T_{S;6.9}^V$, and at 10.7 GHz, $T_{S;10.7}^V$, and we keep the AMSR-E surface wind (U_{10}), columnar cloud liquid water (CLW) and the columnar Water vapor (WV), as well as the spatially averaged and re-gridded CCI-SST for further empirical adjustments.

In parallel, the expected flat ocean surface reflectance (X- minus C-band) contrasts were estimated using the dielectric constant model for sea water of Meissner and Wentz (2004,2006) applied to L-band based CCI v2.31 SSS and CCI-SST fields that were collected over Jan 2010-Sep 2011 in the four regions. For these 21 common months, AMSR-E surface datasets were compared to the CCI-based modeled surface Tbs to further determine empirical corrections for

- Surface wind speed dependent contributions. To characterize and correct for the impact of sea surface roughness separately on C-, and X-band surface brightness in V-polarization, one could use already developed Geophysical Model Functions of the isotropic wind induced sea surface emissivity ([Meissner and Wentz 2006](#)), and of the wind directional signal impact on the sea surface emissivity ([Meissner and Wentz 2002](#)) and ([Meissner and Wentz 2006](#)). However, we found some discrepancies in the highest wind speed regimes (> 12 m/s) between these GMFs and the residuals observations we obtained after performing all corrections except for roughness. Using the differences between the specular sea surface emissivity model and AMSR-E estimates, empirical GMFs of the wind induced isotropic contribution to emissivity were derived for C and X band and are used here to correct for the roughness effect on surface emissivity. In a first step, we neglected the wind directional signal of the sea surface emissivity.
- Correction of residuals signals as function of SST, WV and CLW. Additional empirical corrections are finally applied to correct for residual biases as a function of first SST and then columnar water vapor V and columnar cloud liquid content L . These empirical corrections were derived as follows for each C- and X- band frequency of AMSR-E. The specular sea surface emission was evaluated using CCI SST and CCI L-band -based SSS (v2.31) products for 21 months from January 2010 to September 2011. The AMSR-E surface Tbs corrected for atmospheric effects including downwelling radiation scattering effects and corrected for the isotropic rough sea surface emission were evaluated using the RTM. These residual specular emission quantity were collected for all four regions together and binned as function of CCI SST. As found, after applying the full RTM corrections, residual systematic biases as a function of SST are found with differing behaviour at each electromagnetic frequency. Empirical fits were derived to correct for these residual biases

4.1.3.5 Step 5: Land Sea Contamination and outliers removal



To filter the land-sea contamination, we apply a spatial filter by removing data which show higher Median Absolute Deviation (MAD) of the $\Delta\epsilon$ in one pass direction than in the other and determined over the full AMSR-E archive (May 2002-October 2011). To this aim, we defined a mask where the difference of the temporal MAD for ascending data is greater than +0.06K (equivalent of 1.2 psu) and for the descending data where the difference is less than -0.06 K, creating two static masks applied separately for ascending and descending flat surface $\Delta\epsilon$ data.

Once the land contamination mask has been applied, we scan the remaining ΔT_B time series at each location to exclude potential outliers such as the one from unfiltered Radio Frequency Interferences. The temporal median and Mean Absolute Deviation (MAD) of ΔT_B is re-evaluated in $\frac{1}{4}^\circ \times \frac{1}{4}^\circ$ boxes, separately for A and D direction, over May 2002-October 2011. Outliers (more than 3 MAD away from the median) are then filtered out. After these two filtering steps steps, the difference in the MAD of the A and D passes is less than 0.02K (0.4 pss)

4.1.3.6 Neural Network inversion algorithm

This part of the algorithm provides the SSS retrieval methodology from inputs of the filtered sea surface emissivity frequency differential contrasts Δe_{surf}^{spec} , SST, wind, WV and CLW.

4.2 Input data for CCI+SSS from AMSR-E C/X-bands

4.2.1 AMSR-E/Aqua L2A Global Swath Spatially-Resampled Brightness Temperatures

The AMSR-E Level-2A product (AE_L2A) contains daily 50 minute half-orbit swath brightness temperatures for six channels ranging from 6.9 GHz through 89 GHz. Data are resampled to spatial resolutions ranging from 5.4 km to 56 km. We use the low resolution (~56 km) data associated to the C-band channels. Each file is packaged with geolocation and quality information as well as ancillary data. We use the Version 4 L2A data distributed by the National Snow and Ice Data Center (NSIDC) at https://nsidc.org/data/AE_L2A

4.2.2 AMSR-E/Aqua L2B Global Swath Ocean Products

The algorithm also uses as input the AMSR-E/Aqua L2B Global Swath Ocean Products derived from Wentz Algorithm, Version 2. This daily Level-2B swath data set includes Sea Surface Temperature (SST), Near-Surface Wind Speed, Columnar Water Vapor, and Cloud liquid Water data arrays retrieved from the L2A brightness temperatures. We use the Version 2 L2B data distributed by the National Snow and Ice Data Center (NSIDC) at https://nsidc.org/data/ae_ocean/versions/2

Input variable



$T_{A;6.9}^V$	L2A daily 50 minute half-orbit swath Calibrated & Resampled Antenna Brightness Temperature in V-polarization at 6.9 GHz	Kelvins
$T_{A;10.7}^V$	L2A daily 50 minute half-orbit swath Calibrated & Resampled Antenna Brightness Temperature in V-polarization at 10.7 GHz	Kelvins
EIA	Earth Incidence Angle	Degrees
EAA	Earth Azimut Angle	Degrees
Sun_Glint_Angle	Angle between sun specular direction and radiometer viewing angle	Degrees
lat	Latitude of footprint center	Degrees N
lon	Longitude of footprint center	Degrees
time	UTC time of aquisition	
wind	L2B near surface wind speed	Meter per seconds
sst	L2B Sea Surface Temperature	Degree Celcius
vapor	L2B Columnar water vapor	mm
clwc	L2B Columnar cloud liquid water	mm
Ocean_products_quality_flag	Ensemble of ocean flags	
rain_flag	Ensemble of rain flags	
land_flag	Ensemble of land flags	

4.3 Radiative Transfer Model (RTM)

4.3.1 Top of the Atmosphere Brightness temperature

The general RTM expression for the Top Of the Atmosphere (TOA) TB of polarization $p=v,h$ and frequency f is (Meissner and Wentz, 2012):

$$T_{B,p} = T_{BU} + \tau \cdot E_p \cdot T_S + \tau \cdot T_{B\Omega} \quad (1)$$

where $T_{B\Omega} = R_p \cdot [T_{BD} + \tau \cdot T_{cold}] + T_{B,,scat,p}$

Here T_S denotes the SST, E_p the total sea surface emissivity at frequency f , $R_p = 1 - E_p$ the sea surface reflectivity, τ the atmospheric transmittance, T_{BU} the upwelling atmospheric brightness temperature, T_{BD} the downwelling atmospheric brightness temperature that is reflected at the

ocean surface, T_{cold} the effective cold space temperature after taking into account the deviation from the Rayleigh-Jeans approximation (Meissner and Wentz, 2010). The term $\tau \cdot T_{B,scat,p}$ accounts for the atmospheric path length correction in the downwelling scattered sky radiation (see details further).

4.3.2 Atmospheric contributions

For atmospheres without rain where scattering can be neglected, the atmospheric parts τ_f (atmospheric transmittance), T_{BU} (upwelling atmospheric brightness temperature) and T_{BD} (downwelling atmospheric brightness temperature) can be calculated from the atmospheric profiles of temperature $T(s)$ and the absorption coefficient $\alpha(s)$:

$$T_{BU} = \int_0^{TOA} \alpha(s)T(s)\tau(s, TOA) ds$$

$$T_{BD} = \int_0^{TOA} \alpha(s)T(s)\tau(s, 0) ds$$

$$\tau(s_1, s_2) = \exp\left[-\int_{s_1}^{s_2} \alpha(s) ds\right] \quad (2)$$

In the equations above, s is the path length along the propagation of the electromagnetic ray with $s = 0$ being the ocean surface and $s = TOA$ the TOA. $\tau_f(s_1, s_2)$ is therefore the transmittance between points s_1 and s_2 along the propagation path. The total transmittance is $\tau_f = \tau_f(0, TOA)$. Following Meissner and Wentz, (2012), we will use a 1-dimensional RTM, which means that the atmospheric temperature is assumed to be horizontally uniform and depends only on the altitude h above the surface. The transformation between s and h in the integrals of (2) is:

$$\frac{\partial s}{\partial h} = \frac{1+\delta}{\sqrt{\cos^2 \theta_i + \delta(2+\delta)}} \quad (3)$$

Where θ_i is the earth incidence angle (EIA). $\delta = h/R_E$, and R_E is the radius of the Earth. In the troposphere $\delta \ll 1$, and an excellent approximation for $\theta_i < 60^\circ$ is

$$\frac{\partial s}{\partial h} \approx \frac{1.00035}{\sqrt{\cos^2 \theta_i + 7.001225 \cdot 10^{-4}}} \approx \sec \theta_i$$

With this approximation and the assumption of horizontal uniformity, if $h=H$ is the altitude of TOA, the above equations reduce to the following expressions:

$$\tau(h_1, h_2, \theta_i) = \exp \left[-\sec\theta_i \int_{h_1}^{h_2} \alpha(h) dh \right] \quad (4)$$

$$\tau = \tau(0, H, \theta_i) \quad (5)$$

$$T_{BU} = \sec\theta_i \int_0^H \alpha(h) T(h) \tau(h, H, \theta_i) dh \quad (6)$$

$$T_{BD} = \sec\theta_i \int_0^H \alpha(h) T(h) \tau(0, h, \theta_i) dh \quad (7)$$

Thus, the estimation of the above atmospheric contributions to the antenna brightness temperature requires the vertical profiles of atmospheric temperature $T(h)$ and the vertical profile of the atmospheric absorption $\alpha(h)$.

Determination of the Atmospheric Absorption $\alpha(h)$.

For the microwave frequencies under consideration, the atmospheric absorption coefficient has three contributions: : oxygen, water vapor, and liquid water in the form of clouds and rain [Waters, 1976].

The sum of these three components gives the total absorption coefficient (neppers/cm)

$$\alpha(h) = \alpha_L(h) + \alpha_V(h) + \alpha_O(h) \quad (8)$$

Numerous investigators have studied the dependence of the oxygen and water vapor coefficients on frequency f (GHz), temperature T (K), pressure P (mb), and water vapor density ρ_V (g/cm³) [Becker and Autler, 1946; Rozenkranz, 1975; Waters, 1976; Liebe, 1985]. To specify α_O and α_V as a function of (f, T, P, ρ_V) we use the Liebe [1985] expressions with one modification. The self-broadening component of the water vapor continuum is reduced by a factor of 0.52 The liquid water coefficient α_L comes directly from the Rayleigh approximation to Mie scattering and is a function of T and the liquid water density ρ_L (g/cm²).

The computation of the atmospheric parts τ , T_{BU} , and T_{BD} of the RTM function (1) can be done in different ways. The most accurate but also most computation intensive method is to use atmospheric profiles for T , p , ρ_V and ρ_L , scale both ρ_V and ρ_L by the values of the total columnar integrals V and L , respectively, and then perform the numerical integrals in (2). A simplified approach, which was followed in [Meissner & Wentz, 2012] and that we follow also here, is to take typical ocean-atmosphere scenes derive analytic expressions for τ , T_{BU} , and T_{BD} as function of $T(s)$ and the columnar values V and L , that were retrieved from the Level 2B ocean products.

Let A_I denote the vertically integrated absorption coefficient.

$$A_I = \int_0^H \alpha_I(h) dh \quad (9)$$

Where h is the height (cm) above the Earth's surface and subscript I equals O (oxygen), V (vapor), or L (cloud liquid water). Equations (4) and (5) then give the total transmittance to be



$$\tau = \exp[-\sec\theta_i(A_O + A_V + A_L)] \quad (10)$$

Assuming for the moment that the atmospheric temperature is constant with height and equal to the SST, i.e., $T(h) = T = T_S$, then the integrals in equations (4-11) can be exactly evaluated in closed form to yield :

$$T_{BU} = T_{BD} = (1 - \tau)T \quad (11)$$

In view of (11), we find it convenient to parameterize the atmospheric model in terms of the following upwelling and downwelling effective air temperatures:

$$T_U = T_{BU}/(1 - \tau)$$
$$T_D = T_{BD}/(1 - \tau)$$

These effective temperatures are indicative of the air temperature averaged over the lower to mid troposphere. Note that in the absence of significant rain, T_U and T_D are very similar in value, with T_U being 1 to 2 K colder. In view of the above equations, one sees that the atmospheric model can be parameterized in terms of the following 5 parameters:

1. Upwelling effective temperature T_U
2. Downwelling effective temperature T_D
3. Vertically integrated oxygen absorption A_O
4. Vertically integrated water vapor absorption A_V
5. Vertically integrated liquid water absorption A_L

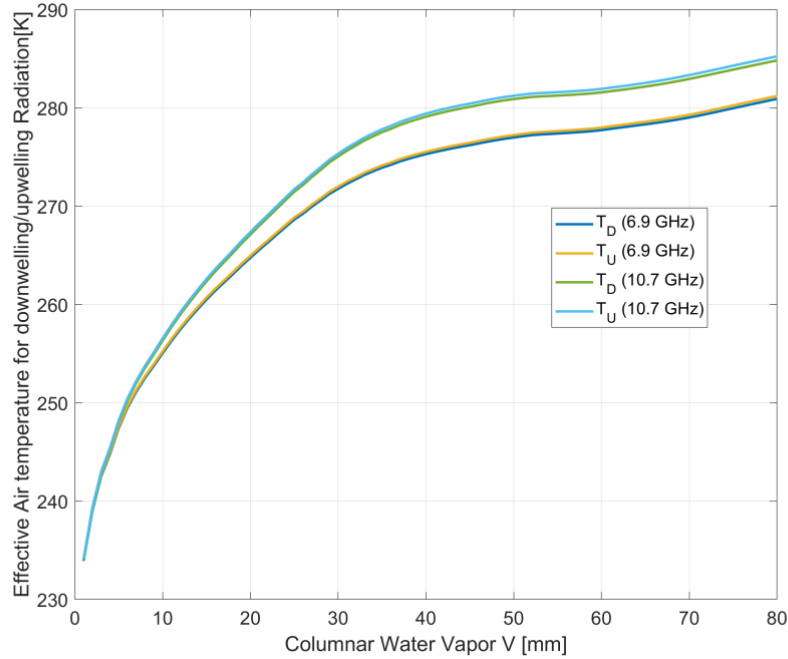


Figure 11: Meissner and Wentz's (2012) model of the effective air temperature for upwelling T_D and downwelling T_U radiation as a function of the vertically integrated Columnar water vapor V . The curves are provided for both C- and X- band frequencies

As determined from radiosonde observation in Wentz (2000), for low to moderate values of V (0 to 40 mm), T_D increases with V , and above 40 mm, T_D reaches a relatively constant value and then re-increase again above 60 mm. The T_U versus V curves are very similar except that T_U is 1 to 2 K colder. Least-square regressions are found to be a good approximation of the T_D, T_U , versus V relationship:

$$T_D = b_0 + b_1 \cdot V + b_2 \cdot V^2 + b_3 \cdot V^3 + b_4 \cdot V^4 + b_5 \cdot \zeta(T_S - T_V) \quad (12a)$$

$$T_U = T_D + b_6 + b_7 \cdot V \quad (12b)$$

	f=6.9 GHz	f=10.7 GHz
b_0	239.5	239.51
b_1	213.92e-2	225.19e-2
b_2	-460.6e-4	-446.86e-4
b_3	457.11e-6	391.82e-6
b_4	-16.84e-7	-12.2e-7
b_5	0.5	0.54
b_6	-0.11	-0.12
b_7	-0.21e-2	-0.34e-2

The computation of T_V , representing a sea surface temperature that is typical for water vapor V follows:

$$T_V = 273.16 + 0.8337 \cdot V - 3.029 \cdot 10^{-5} \cdot V^{3.33} \quad \text{for } V \leq 48 \text{ mm} \quad (12c)$$



$$T_V = 301.16 \quad \text{for } V > 48 \text{ mm} \quad (12d)$$

The term $\zeta(T_S - T_V)$ accounts for the fact that the effective air temperature is typically higher (lower) for the case of unusually warm (cold) water.

$$\zeta(T_S - T_V) = 1.05 \cdot (T_S - T_V) \cdot \left(1 - \frac{(T_S - T_V)^2}{1200}\right) \quad \text{for } |T_S - T_V| \leq 20K \quad (12f)$$

$$\zeta(T_S - T_V) = \text{sign}(T_S - T_V) \cdot 14K \quad \text{for } |T_S - T_V| > 20K \quad (12e)$$

The coefficients α_o and α_V are computed from the *Liebe* [1985] expressions, except that the water vapor continuum term is modified. The vertically integrated oxygen absorption A_o is nearly constant over the globe, with a small dependence on the air temperature and can be approximated using:

$$A_o = a_{o1} + a_{o2}(T_D - 270) \quad (13)$$

The coefficients $a_{o1,2}$ for both C and X-band channels of AMSR-E are

	f=6.9 GHz	f=10.7 GHz
a_{o1}	8.34e-3	9.08e-3
a_{o2}	-0.48e-4	-0.47e-4

The vapor absorption A_V is primarily a linear function of V , although there is a small second order term:

$$A_V = a_{V1} + a_{V2} \cdot V^2 \quad (14)$$

The coefficients $a_{V1,2}$ for both C and X-band channels of AMSR-E are

	f=6.9 GHz	f=10.7 GHz
a_{V1}	0.07e-3	0.18e-3
a_{V2}	0.001e-5	0.001e-5

The liquid cloud water absorption profile α_L depends on atmospheric temperature and liquid cloud water density $\rho_L(h)$ (in grams per cubic centimetre). For nonraining atmospheres, it can be treated using Rayleigh approximation:

$$\alpha_L(h) \approx \frac{6\pi\rho_L(h)}{\lambda \cdot \rho_o} \cdot \text{Im} \left[\frac{1-\varepsilon}{2+\varepsilon} \right] \quad (15)$$

where $\lambda = c/f$ is the radiation wavelength (in centimeters) and $\rho_o \approx 1.0 \text{ g/cm}^3$ is the density of water. ε is the dielectric constant of pure (cloud) water, which depends on the radiation frequency f and the cloud temperature T . For its computation, we use the dielectric model of Meissner and Wentz (2004) as detailed in 4.3.3.2.1. Substituting (15) into (9) gives

$$A_L = \frac{0.6\pi L}{\lambda} \cdot \text{Im} \left[\frac{1-\varepsilon}{2+\varepsilon} \right] \quad (16)$$



where L is the vertically integrated liquid water (mm) given by the input L2B products. A very good approximation of (16) is:

$$A_L = a_{L1}[1 - a_{L2}(T_L - 283)]L \quad (17)$$

where T_L is the mean temperature of the cloud, approximated by

$$T_L = (T_S + 273)/2 \quad (18)$$

which is the mean temperature between the surface and the freezing level.

and the $a_{L1,2}$ coefficients are given by:

The coefficients $a_{V1,2}$ for both C and X-band channels of AMSR-E are

	f=6.9 GHz	f=10.7 GHz
a_{L1}	0.0078	0.0183
a_{L2}	0.0303	0.0298

In practice in our algorithm, we generated Look-Up Tables (LUTs) for estimating the five atmospheric parameters T_U, T_D, A_O, A_V, A_L from input values of the sst (T_S), columnar water vapor (V), and columnar cloud liquid water (L).

4.3.3 Sea Surface Emission

E_p the total sea surface emissivity is the sum of two terms:

$$E_p = E_{o,p} + \Delta E_{p,rough} \quad (19)$$

Where $E_{o,p}$ is the specular sea surface emission and $\Delta E_{p,rough}$ is the roughened sea surface emission contribution. We detail these two models hereafter.

4.3.3.1 Specular sea surface Emission contribution

For a perfectly flat ocean surface the scattered electric and magnetic fields may be expressed in terms of the incident fields. The reflected electric field components (E'_h, E'_v) are related to the incident components (E_h, E_v) by the diagonal matrix equation:

$$\begin{pmatrix} E'_h(\theta_s, \phi_s) \\ E'_v(\theta_s, \phi_s) \end{pmatrix} = \begin{pmatrix} R_{hh}^{(0)} & 0 \\ 0 & R_{vv}^{(0)} \end{pmatrix} \begin{pmatrix} E_h(\theta_s, \phi_s - 180^\circ) \\ E_v(\theta_s, \phi_s - 180^\circ) \end{pmatrix}$$

Where (θ_s, ϕ_s) is the specular reflection direction for radiation incident from direction $(\theta_i = \theta_s, \phi_i = \phi_s - 180^\circ)$. The superscripts on the reflection coefficients indicate that they

correspond to zero order expansion in surface slope, i.e., the flat surface reflection. The flat surface reflection coefficients on the preceding matrix are given by the Fresnel equations:

$$R_{hh}^{(0)}(S, T_s, \theta_s) = \frac{\cos \theta_s - \sqrt{\epsilon_{sw}(S, T_s) - \sin^2 \theta_s}}{\cos \theta_s + \sqrt{\epsilon_{sw}(S, T_s) - \sin^2 \theta_s}} \quad (20a)$$

$$R_{vv}^{(0)}(S, T_s, \theta_s) = \frac{\epsilon_{sw}(S, T_s) \cos \theta_s - \sqrt{\epsilon_{sw}(S, T_s) - \sin^2 \theta_s}}{\epsilon_{sw}(S, T_s) \cos \theta_s + \sqrt{\epsilon_{sw}(S, T_s) - \sin^2 \theta_s}} \quad (20b)$$

Where $\epsilon_{sw}(S, T_s, f)$ is the dielectric constant for seawater, which is a function of the surface salinity S and temperature T_s as well as the electromagnetic frequency. We use the Meissner et al. (2012)'s dielectric constant model for the C- and X-band data. The Fresnel reflection matrix equation is:

$$T' = \begin{pmatrix} T'_h \\ T'_v \\ U' \\ V' \end{pmatrix} = M^{(0)} T = \begin{pmatrix} |R_{hh}^{(0)}|^2 \delta^2 & 0 & 0 & 0 \\ 0 & |R_{vv}^{(0)}|^2 \delta^2 & 0 & 0 \\ 0 & 0 & \Re \{ R_{hh}^{(0)} (R_{vv}^{(0)})^* \} & \Im \{ R_{hh}^{(0)} (R_{vv}^{(0)})^* \} \\ 0 & 0 & -\Im \{ R_{hh}^{(0)} (R_{vv}^{(0)})^* \} & \Re \{ R_{hh}^{(0)} (R_{vv}^{(0)})^* \} \end{pmatrix} \begin{pmatrix} T_h \\ T_v \\ U \\ V \end{pmatrix}$$

For the linear polarizations, the Fresnel power reflection coefficients are thus:

$$|R_{hh}^{(0)}(S, T_s, \theta_s)|^2 = \left| \frac{\cos \theta_s - \sqrt{\epsilon_{sw}(S, T_s) - \sin^2 \theta_s}}{\cos \theta_s + \sqrt{\epsilon_{sw}(S, T_s) - \sin^2 \theta_s}} \right|^2$$

$$|R_{vv}^{(0)}(S, T_s, \theta_s)|^2 = \left| \frac{\epsilon_{sw}(S, T_s) \cos \theta_s - \sqrt{\epsilon_{sw}(S, T_s) - \sin^2 \theta_s}}{\epsilon_{sw}(S, T_s) \cos \theta_s + \sqrt{\epsilon_{sw}(S, T_s) - \sin^2 \theta_s}} \right|^2$$

The specular emission in horizontal polarization can then be estimated :

$$E_{o,h}(S, T_s, \theta_i) = T_s \left[1 - |R_{hh}^{(0)}(\epsilon_{sw}, \theta_i)|^2 \right] \quad (21)$$

and in vertical polarization:

$$E_{o,v}(S, T_s, \theta_i) = T_s \left[1 - \left| R_{vv}^{(0)}(\epsilon_{sw}, \theta_i) \right|^2 \right] \quad (22)$$

4.3.3.2 Dielectric Constant of pure and Sea Water

The model for ϵ , the dielectric constant of water, depends on the radiation frequency f , the water temperature T and the salinity S of the sample. ϵ for pure water is used in Equation (9) to derive the vertically integrated liquid cloud water absorption and for salty water in (14-15). Following Meissner and Wentz (2004), the dielectric constant of water is fitted using a double relaxation law. The general form reads:

$$\epsilon(T, S) = \frac{\epsilon_S(T, S) - \epsilon_1(T, S)}{1 + i\nu/\nu_1(T, S)} + \frac{\epsilon_1(T, S) - \epsilon_\infty(T, S)}{1 + i\nu/\nu_2(T, S)} + \epsilon_\infty(T, S) - i \frac{\sigma(T, S)}{(2\pi\epsilon_0)\nu} \quad (23)$$

Here:

- $i = \sqrt{-1}$, ν is the radiation frequency [in GHz],
- The temperature T is in °C and the salinity S in pss
- $\epsilon_S(T, S)$ is the static (zero frequency) dielectric constant
- $\epsilon_\infty(T, S)$ is the dielectric constant at infinite frequencies
- $\epsilon_1(T, S)$ is the intermediate frequency dielectric constant.
- $\nu_1(T, S)$ and $\nu_2(T, S)$ are the first and second Debye relaxation frequencies [in GHz], respectively
- $\sigma(T, S)$ is the conductivity of water in [S/m]
- $\epsilon_0 = 8.854 \cdot 10^{-12}$ is [F/m] is the vacuum electric permittivity

4.3.3.2.1 Dielectric Constant of Pure Water

In this section we will consider pure water where $S = 0$ and $\sigma(T, S = 0) = 0$. The dielectric constant for pure water then reads:

$$\epsilon(T, S = 0) = \frac{\epsilon_S(T, S = 0) - \epsilon_1(T, S = 0)}{1 + i\nu/\nu_1(T, S = 0)} + \frac{\epsilon_1(T, S = 0) - \epsilon_\infty(T, S = 0)}{1 + i\nu/\nu_2(T, S = 0)} + \epsilon_\infty(T, S = 0)$$

The static dielectric constant for pure water $\epsilon_S(T, S = 0)$ is given by:

$$\epsilon_S(T, S = 0) = \frac{3.70886 \cdot 10^4 - 8.2168 \cdot 10^1 T}{4.21854 \cdot 10^2 + T}$$

For the temperature dependence of the 4 fit parameters ϵ_1 , ϵ_∞ , ν_1 and ν_2 , we use:

$$\epsilon_1(T, S = 0) = a_0 + a_1 T + a_2 T^2$$

$$v_1(T, S = 0) = \frac{45 + T}{a_3 + a_4T + a_5T^2}$$

$$\varepsilon_\infty(T, S = 0) = a_6 + a_7T$$

$$v_2(T, S = 0) = \frac{45 + T}{a_8 + a_9T + a_{10}T^2}$$

The parameters for the fits are given by

$$a_0 = 5.723; \quad a_1 = 2.2379e - 2; \quad a_2 = -7.1237e - 4; \quad a_3 = 5.0478; \quad a_4 = -7.0315e - 2;$$

$$a_5 = 6.0059e-4; \quad a_6 = 3.6143; \quad a_7 = 2.8841e-2; \quad a_8 = 1.3652e-1; \quad a_9 = 1.4825e-3; \quad a_{10} = 2.4166e - 4$$

4.3.3.2.2 Dielectric Constant of Sea Water

For sea water, a model for the conductivity of sea water $\sigma(T, S)$ is needed:

$$\sigma(T, S) = \sigma(T, S = 35) \cdot R_{15}(S) \cdot \frac{R_\tau(S)}{R_{15}(S)}$$

Where with the units: T [°C], S [pss], and σ [S/m]:

$$\sigma(T, S = 35) = 2.903602 + 8.607 \cdot 10^{-2} \cdot T + 4.738817 \cdot 10^{-2} \cdot T^2 - 2.991 \cdot 10^{-6} \cdot T^3 + 4.3047 \cdot 10^{-9} \cdot T^4$$

$$R_{15}(S) = S \cdot \frac{(37.5109 + 5.45216 \cdot S + 1.4409 \cdot 10^{-2} \cdot S^2)}{(1004.75 + 182.283 \cdot S + S^2)}$$

$$\frac{R_\tau(S)}{R_{15}(S)} = 1 + \frac{\alpha_o(T - 15)}{(\alpha_1 + T)}$$

$$\alpha_o(S) = \frac{(6.9431 + 3.2841 \cdot S - 9.9486 \cdot 10^{-2} \cdot S^2)}{(84.850 + 69.024 \cdot S + S^2)}$$

$$\alpha_1(S) = 49.843 - 0.2276 \cdot S + 0.198 \cdot 10^{-2} \cdot S^2$$

For the remaining five constants in Equation (12), we use the following expressions:

$$\varepsilon_s(T, S) = \varepsilon_s(T, S = 0) \cdot \exp[b_0S + b_1S^2 + b_2TS]$$

$$v_1(T, S) = v_1(T, S = 0) \cdot [1 + S \cdot (d_0 + d_1T + d_2T^2 + d_3T^3 + d_4T^4)]$$

$$\varepsilon_1(T, S) = \varepsilon_1(T, S = 0) \cdot \exp[b_6S + b_7S^2 + b_8TS]$$



$$v_2(T, S) = v_2(T, S = 0) \cdot [1 + S \cdot (b_9 + b_{10}T)]$$

$$\varepsilon_\infty(T, S) = \varepsilon_\infty(T, S = 0) \cdot [1 + S \cdot (b_{11} + b_{12}T)]$$

We followed the changed made in Meissner and Wentz (2012), with respect Wentz (2000) algorithm with the parameters of the fits given by:

$$b_0 = -3.3333e-3; b_1 = 4.74868e-6; b_2 = 0;$$

$$d_0 = 0.23232e-2; d_1 = -0.79208e-4; d_2 = 0.36764e-5; d_3 = 0.35594e-6; d_4 = 0.89795e-8;$$

$$b_6 = -6.28908e-3; b_7 = 1.76032e-4; b_8 = -9.22144e-5; b_9 = -1.99723e-2; b_{10} = 1.81176e-4; b_{11} = 2.04265e-3; b_{12} = 1.57883e-4;$$

4.3.3.3 Rough sea surface emission

The brightness temperature of the sea surface is expressed as follows:

$$E_{p,f}^{surf} = [E_{o,p}(T_S, S, f, p, \theta) + \Delta E_{rough,p}(U_{10}, \varphi_r, \theta, f)] \quad (24)$$

and is the sum of two contributions to the total surface emissivity:

- E_o : the specular sea surface emission defined in (14) and (15), and,
- $\Delta E_{rough,p}$: the rough and foamy sea surface emission which is expressed as a function of the 10 m height ocean surface wind speed U_{10} and the relative direction φ_r following:

$$\Delta e_{rough,p}(U_{10}, \theta, \varphi_r) = \Delta e_{o,p}(U_{10}, \theta) + \Delta e_{1,p}(U_{10}, \theta) \cdot \cos(\varphi_r) + \Delta e_{2,p}(U_{10}, \theta) \cdot \cos(2\varphi_r) \quad p=H,V \quad (25)$$

In these expression: $\varphi_r = \varphi_w - \alpha$, where φ_w is the wind direction and α the radiometer azimuthal look direction relative to North.

4.3.3.3.1 Isotropic components of the wind-induced emission at C- and X-bands

In the present algorithm, we use an empirical model of the C- and X-band isotropic roughness-induced emission in V-polarization $\Delta e_{o,V}(U_{10})$. These empirical fits were derived as follows for each C- and X- band frequency of AMSR-E. The specular sea surface emission was evaluated using CCI SST and CCI L-band -based SSS (v2.31) products as inputs to Equation (22) for 21 months from January 2010 to September 2011. The AMSR-E Tbs were corrected for atmospheric effects including downwelling radiation scattering effects (see next section) and for the specular sea emission determined from CCI data to estimate the residual roughness-induced emission in V-polarization $\Delta e_{o,V}(U_{10})$. This quantity was collected for all four regions together and binned as function of AMSR-E L2B surface wind speed to derive the following empirical fits:

$$\Delta e_{o,V}(U_{10}) = \sum_{i=1}^4 a_{oi,V} \cdot U_{10}^i \quad (25)$$

Where the $a_{oi,V}$ coefficients for the zeroth azimuthal harmonics are given here below:

Table 3: Isotropic roughness emissivity coefficients $a_{oi,V}$ for the C- and X-band frequencies and V polarization

f [GHz]	i=0	i=1	i=2	i=3	i=4
6.8	0.0024	-0.0014	1.5666e-04	-9.8011e-07	-5.0347e-08
10.7	0.0023	-0.0015	1.8440e-04	-2.4595e-06	-1.0507e-08

These GMFs function are plotted in **Figure 12**. As found the V-pol brightness temperature change induced by increasing wind is very similar between C and X-bands for winds below 15 m/s. At higher winds, X-band emissivity is higher than C-band and might generate a differential signal between both frequencies that can be corrected using (25).

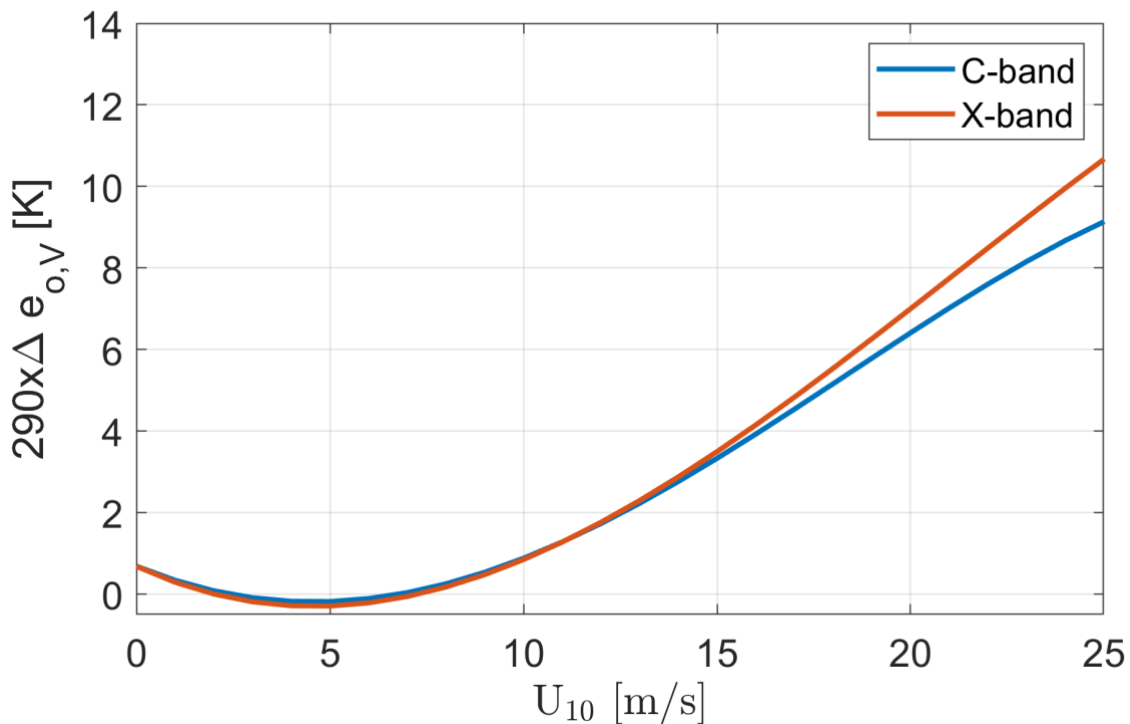


Figure 12: Isotropic components of the wind-induced emission at C- and X-band and Vertical Polarization

4.3.3.3.2 Anisotropic components of the wind-induced emission at C- and X-bands

The wind direction signal of the sea surface brightness temperature comes from the 1st harmonic term $\Delta e_{1,p}$ and the 2nd harmonic term $\Delta e_{2,p}$. The different mechanisms responsible for sea surface emissivity in the microwave domain exhibit several anisotropic features, which, in turn, lead to a wind directional dependence of the observed brightness temperatures. The probability density function of the sea surface slope is skewed in the along wind axis and has a larger along wind variance than crosswind variance (Cox, 1958). Furthermore, the RMS height of the small gravity-



capillary waves, which are riding on top of the large gravity waves, exhibits a noticeable anisotropy. The gravity-capillary waves traveling in the along-wind direction have larger amplitudes than those traveling in the crosswind direction (Mitsuyasu and Honda, 1982). Both effects cause an up-crosswind asymmetry of the emitted radiation. In addition, up-downwind asymmetries occur. The gravity-capillary waves and sea foam are not uniformly distributed over the underlying structure of large-scale waves. Aircraft radiometer measurements (Smith, 1988) show that the forward plunging side of a breaking wave is emitting warmer microwave emissions than its backside. Furthermore, the small-scale gravity-capillary waves have the tendency to cluster on the downwind side of the large-scale gravity waves (Cox, 1958; Keller and Wright, 1975). Finally, several studies of nonlinear wave-wave interaction suggest that the small-scale ocean surface waves are not propagating in the wind direction (Banner and Young, 1994; . Young et al., 1995; Ewans, 1998; Hwang et al., 2000; Irisov, 2000; Hwang and Wang, 2001). This might be an additional source of error in the wind direction retrieval from radiometer data. Nevertheless, based on SMAP, Aquarius, SMOS, WindSat data, empirical model for the anisotropic components of sea surface emissivity have been derived.

The C- and X-band azimuthal anisotropic **harmonic coefficients** $\Delta e_{k,p}(U_{10})$ were derived by Meissner et al. (2012) and follows:.

$$\Delta e_{k,p}(U_{10}) = \sum_{i=1}^5 a_{ki,p} \cdot U_{10}^i$$

Where the $a_{ki,p}$ coefficients for the first and second azimuthal harmonics are given here below:

Table 4: First azimuthal harmonic coefficients $a_{1i,p}$ for the C- and X-band frequencies and V-polarization

f [GHz]	p	i=1	i=2	i=3	i=4	i=5
6.8	V	4.46633E-07	3.34314E-07	3.12587E-06	-1.99336E-07	3.55175E-09
10.7	V	4.96132E-05	-2.90991E-05	9.05913E-06	-5.73703E-07	1.10332E-08

Table 5: Second azimuthal harmonic coefficients $a_{2i,p}$ for the C- and X-band frequencies and V-polarization

f [GHz]	p	i=1	i=2	i=3	i=4	i=5
6.8	V	2.21863E-04	-1.18053E-04	1.68718E-05	-8.94076E-07	1.60273E-08

10.7	V	1.48213E-04	-7.15954E-05	1.01992E-05	-5.41575E-07	9.71451E-09
------	---	-------------	--------------	-------------	--------------	-------------

The directional dependence of the excess surface emissivity at C and X band is small for low winds and it increases with increasing wind speed. There is larger first harmonic amplitude for vertical polarization than for horizontal polarization at all frequencies. The first harmonic amplitude is also in general significantly higher than the second harmonic amplitude. The relative polarization behavior is consistent with the characteristics of high-frequency observations (Yueh et al., 1999; Piepmeier and Gasiewski, 2001; Yueh et al., 2006). At a wind speed of 20 m/s, the peak-to-peak change of $\Delta e_{1,V}(U_{10})$ is about 1.5 K at C and X-bands in brightness temperature and increase to 3-4 K (C/X-bands) at 50 m/s. The second harmonic coefficients $\Delta e_{2,p}(U_{10})$ are generally quite small for wind speeds less than 10 m/s except in H-polarization and X-band where it reaches ~ 1 K at 20 m/s. In between 10 m/s and 15 m/s, $\Delta e_{2,V}(U_{10})$ appears to increase linearly until the wind speed reaches 15 m/s, while $\Delta e_{2,H}(U_{10})$ appears to vary in opposite phase to $\Delta e_{2,V}(U_{10})$. Note that the behaviour of the first and second harmonic coefficients at the highest winds > 20 m/s is rather uncertain. Some authors advise to keep the coefficient values constant at winds higher than 20 m/s (Meissner et al., 2014), some author advise to linearly interpolate the later in the wind speed range (e.g., Yueh et al., 2013).

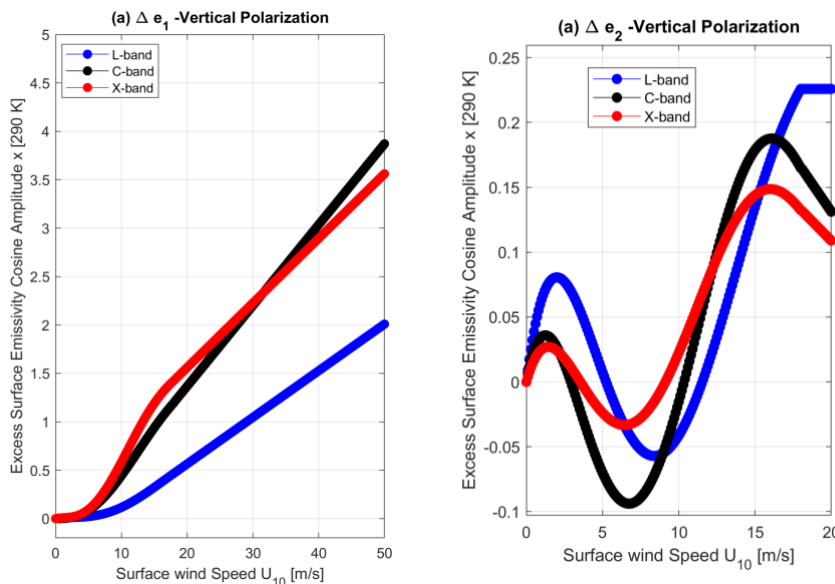


Figure 13: GMF of the first (left) and second (right) azimuthal harmonic coefficients $\Delta e_{1,V}(U_{10})$ as a function of surface wind speed for L- (blue), C-(black) and X-(red) bands.. The values have been multiplied by a common surface temperature of 290 K.

Note: in the present version of the algorithm, for simplicity, we neglected the wind directional dependence of the emissivity at 6.9 GHz and 10.7 GHz. This effect, which can be locally important shall be taken into account but this will be applied in the next ahse-2 version of the algorithm.

4.3.4 Atmospheric and cosmic Radiation Scattered by the Sea Surface

The electromagnetic radiation coming from the ocean surface consists of two parts.

1) The radiation that is directly emitted from the surface, which is the term $E_p \cdot T_S$ in the RTM (1).

2) Downwelling sky radiation (atmospheric and cold space) that is scattered at the ocean surface, which is the term $T_{B\Omega}$ in Eq (1), , where $T_{B\Omega} = R_p \cdot [T_{BD} + \tau \cdot T_{cold}] + T_{B,,scat,p}$

If the surface is rough, this radiation is scattered from a large range of directions θ_s into the incident direction θ_i . The atmospheric path through which this radiation has travelled differs from the atmospheric path if the reflection came only from the incident direction $\theta_s = \theta_i$. This difference in atmospheric path lengths needs to be taken into account in the RTM. There are different ways to do this. If the Kirchhoff law $R_p = 1 - E_p$ is used in (1), a correction needs to be performed, which is formally done in (1) by adding the correction term $\tau \cdot T_{B,,scat,p}$. The effect can be best understood by writing down R_p and $T_{B\Omega}$ in terms of the normalized bistatic cross-sections $\sigma(\vec{k}_s, \vec{k}_i)$ where \vec{k}_s and \vec{k}_i are the scattered and incident wavenumber vectors:

$$R_p(\mathbf{k}_i) = \frac{\sec(\theta_i)}{4\pi} \int_0^{\pi/2} d\theta_s \sin(\theta_s) \int_0^{2\pi} d\varphi_s [\sigma_{\alpha\alpha_i}(\mathbf{k}_s, \mathbf{k}_i) + \sigma_{\alpha_i\alpha}(\mathbf{k}_s, \mathbf{k}_i)]$$

$$T_{B\Omega,p}(\mathbf{k}_i) = \frac{\sec(\theta_i)}{4\pi} \int_0^{\pi/2} d\theta_s \sin(\theta_s) \int_0^{2\pi} d\varphi_s (T_{BD} + \tau \cdot T_{cold}) \times [\sigma_{\alpha\alpha_i}(\mathbf{k}_s, \mathbf{k}_i) + \sigma_{\alpha_i\alpha}(\mathbf{k}_s, \mathbf{k}_i)]$$

Both integrals are over the 2π steradian of the upper hemisphere. If the term $(T_{BD} + \tau \cdot T_{cold})$ in the second integral of $T_{B\Omega,p}(\mathbf{k}_i)$ was independent on direction, it could be taken in front of the integral and one would simply recover that $T_{B\Omega} = R_p \cdot [T_{BD} + \tau \cdot T_{cold}]$, i.e., $T_{B,,scat,p}$ would vanish. However, in general, both terms depend on the atmospheric path length according to (3), and therefore a finite correction term $T_{B,,scat,p}$ needs to be added. This is called the atmospheric path length correction. It is typically parameterized as:

$$T_{B,,scat,p} = \Omega_p(\tau, U_{10}) \cdot [T_{BD} + \tau \cdot T_{cold} - T_{cold}] \cdot R_p$$

Where $\Omega_p(\tau, U_{10} = 0) = 0$ and $\Omega_p(\tau = 0, U_{10}) = 0$. This ansatz automatically guarantees that the $T_{B,,scat}$ vanishes for a smooth surface ($U_{10} = 0$) and for a completely opaque ($\tau = 0$) and a completely transparent ($\tau = 1, T_{BD} = 0$) atmosphere. Opaque and transparent atmospheres are isotropic, and therefore no atmospheric path length correction exists.

The Kirchhoff Approximation (KA) is used to model the bistatic scattering coefficients $\sigma_{\alpha\alpha_i}^0$ from scattering of the incoming plane waves of polarization α_o into the outgoing plane waves of polarization α :



$$\sigma_{\alpha\alpha_i}(\mathbf{k}_s, \mathbf{k}_i) = \frac{1}{\pi} \left| \frac{2q_s q_i}{q_s + q_i} B_{\alpha\alpha_i}(\mathbf{k}_s, \mathbf{k}_i) \right|^2 e^{-(q_s + q_i)^2 \rho(0,0)} \cdot I_K$$

where \mathbf{k}_i and \mathbf{k}_s are the incident and scattered radiation wavenumber vectors, respectively, and, can be expressed in component form as:

$$\mathbf{k}_i / k = (\sin \theta_i \cos \phi_i) \hat{\mathbf{x}} + (\sin \theta_i \sin \phi_i) \hat{\mathbf{y}} + (\cos \theta_i) \hat{\mathbf{z}}$$

$$\mathbf{k}_s / k = (\sin \theta_s \cos \phi_s) \hat{\mathbf{x}} + (\sin \theta_s \sin \phi_s) \hat{\mathbf{y}} + (\cos \theta_s) \hat{\mathbf{z}}$$

where $(\hat{\mathbf{x}}, \hat{\mathbf{y}}, \hat{\mathbf{z}})$ are basis vectors for a local cartesian coordinate system centered at the scattering surface and k is the wavenumber vector magnitude. The Kirchhoff Integral I_K is given in cartesian coordinates by:

$$I_K = \int_{-\infty}^{\infty} \int_{-\infty}^{\infty} \{e^{[(q_s + q_i)^2 \rho(\mathbf{x})]} - 1\} e^{[-i(\mathbf{k}_s - \mathbf{k}_i) \cdot \mathbf{x}]} dx dy$$

The vector \mathbf{x} is the horizontal displacement and the integral is evaluated over all possible displacements on the horizontal plane. $q_s = \hat{\mathbf{z}}_e \cdot \mathbf{k}_s$ and $q_i = -\hat{\mathbf{z}}_e \cdot \mathbf{k}_i$ are the vertical projections of the scattered and incident wavenumbers, respectively; the kernel functions $B_{\alpha\alpha_o}(\mathbf{k}_s, \mathbf{k}_i)$ are functions of both the scattering geometry and the dielectric constant of sea water. Analytical expression of these functions for the Kirchhoff Approximation (KA) can be found in Voronovich and Zavarotny (2001, RD.15). The sea surface elevation function is assumed to be a Gaussian random process, and the correlation function of the ocean surface elevation, $\rho(\mathbf{x})$, is obtained from the Fourier transform of the directional roughness spectrum $W(\mathbf{k})$, which here is given by the wave spectrum model of [RD. 16]. In the present algorithm, only the isotropic part of the spectrum is considered. The computation shows that $T_{B\Omega}$ can be approximated by

$$T_{B\Omega V} = R_p \cdot [(1 + \Omega_p(\tau, U_{10}))(1 - \tau)(T_{BD} - T_{cold}) + T_{cold}] \quad (26)$$

Where the cosmic microwave background temperature $T_{cold} = 2.7 K$. With the KA approximation, the term $\Omega_p(\tau, U_{10}, f)$ is also a function of the microwave frequency f and can be expressed as:

$$\Omega_V(\tau, U_{10}, f) = [2.5 + 0.018 * (37 - f)] \cdot [\Delta S^2 - 70.0 \Delta S^6] \cdot \tau^{3.4} \quad (27)$$

where f is frequency (GHz) and ΔS^2 is the effective sea surface slope variance given by :

$$\Delta S^2 = 5.22 \times 10^{-3} [1 - 0.00748(37 - f)^{1.3}] \cdot U_{10} \quad (28)$$

4.3.5 Frequency differential specular sea surface emissivity contrast

Starting from the RTM equation (1), the TOA $T_{B,p}$ brightness temperature at each frequency reads:

$$T_{B,p} = T_{BU} + \tau \cdot (1 - R_p) \cdot T_S + \tau \cdot R_p \cdot [(1 + \Omega_p(\tau, U_{10})) (1 - \tau) (T_{BD} - T_{cold}) + T_{cold}]$$

and therefore, one express the total surface relectivities in V-polarization as:

$$R_{V,f} = \frac{T_{B,V,f} - T_{BU,f} - \tau_f T_S}{\tau_f [(1 + \Omega_V(\tau, U_{10}, f)) (1 - \tau_f) (T_{BD,f} - T_{cold}) + T_{cold} - T_S]} \quad (29)$$

Where :

- $T_{B,V,f}$ is the input TOA AMSR-E Level-2A TB product (AE_L2A)
- $T_{BU,f}$ is the upwelling brightness temperature and can be estimated using Equation (12b)
- T_S is the sea surface temperature
- τ_f is the atmospheric opacity and can be evaluated using Equation (10)
- $\Omega_V(\tau, U_{10}, f)$ can be evaluated using Equation (27)
- $T_{BD,f}$ is the downwelling brightness temperature estimated using Equation (12a)
- $T_{cold} = 2.7 K$ is the cosmic microwave background temperature

Finally, the perfectly flat surface emitted vertically polarized brightness temperature can then be obtained using:

$$T_{surf,f}^{spec} = T_S [1 - R_{V,f} - \Delta e_{o,f,V}(U_{10})] \quad (30)$$

Where $\Delta e_{o,f,V}(U_{10})$ can be derived from (25). To note, in the approach (30), we neglected the anisotropic impacts of the sea surface roughness on emissivity as they are very similar between C- and X-band for low to moderate winds (see Figure 13).

The frequency differential specular sea surface emissivity contrast between C- and X-band is finally derived from (30) as:

$$\Delta e_{surf}^{spec} = e_{surf,6.9}^{spec} - e_{surf,10.7}^{spec} \quad (31)$$

4.4 AMSR-E SSS retrieval Algorithm

4.4.1 Input Data Filtering

The input data $T_{B,V,f}$ are the TOA AMSR-E Level-2A TB product (AE_L2A) and AMSR-E Level-2B CLW, WV, and U_{10} product (AE_L2B) as well as the SST from CCI project.

Table 9. Resolution Definitions for the Level-2A & B product

Resolution Name	Level-2A Pattern	Antenna	Spatial Resolution	Level-2B Products	Ocean
Very low	6.9 GHz		56 km	SST	
Low	10.7 GHz		38 km	Near-surface speed	wind



Climate Change Initiative+ (CCI+)
Phase 2
 Algorithm Theoretical
 Development Basis Document

Ref.: ESA-CCI-PRGM-EOPS-SW-17-0032
 Date: 15/07/2023
 Version : v4.0
 Page: 62 of 87

Medium	18.7 GHz	21 km	Columnar water vapor
High	36.5 GHz	12 km	Columnar cloud liquid water

The input data $T_{B,V,f}$ are the TOA AMSR-E Level-2A TB product (AE_L2A) and are first filtered to keep only $T_{B,V,f}$ values within the expected range of physical TOA over ocean such that

$$0 < T_{B,V,f} < 320 \text{ K}$$

Some degree of uncertainty is inherent to the input data, namely resampled brightness temperatures, geolocation, and earth incidence angle. Under optimal conditions, additional uncertainty is mainly due to residual errors in the radiative transfer model (RTM) and its inverse, which is essentially the ocean retrieval algorithm. Certain environmental conditions can significantly increase errors and uncertainty, in many cases making some retrievals unfeasible. These environmental factors include land, sea ice, rain, high wind speeds, sun glint, and Radio Frequency Interference (RFI). Some of these factors are stable (land), or at least somewhat consistent (sea ice, rain, winds). Sun glint effects can vary with solar activity, especially solar flare events. RFI is a continuously evolving source of errors.

Low Resolution Wind Speed errors increase with proximity (~50km) to land, sea ice, rain, sun glint specular angle less than ~25°, 11 GHz RFI, and 18 GHz RFI. We therefore filter out the the data if Sun_Glint_Angle <= 25° which is the angle between the spacecraft viewing vector and the sun specular reflection vector. If this angle is smaller than 25°, data corruption might occur.

And we keep only the data over ocean such that the fraction of land in the FOV for C- and X-band channels is less than 0.2%:

$$\text{Land_Ocean_Flag_for_6}==0 \text{ and} \\
\text{Land_Ocean_Flag_for_10}==0.$$

A “Scan_Quality_Flag” is also provided for each scan in the L1 AMSR-E data. These flags pertain to all observations of a scan including all Level-1A and resampled channels. The summary bit 0 of the “Channel_Quality_Flag” in the L2A products is automatically set whenever any of the bits in the “Scan_Quality_Flag” are set. Thus, the user can determine whether the data are useable by examining only the “Channel_Quality_Flag” without examining the Scan_Quality_Flag. We therefore filter the L2A data according to:

$$\text{Channel_Quality_Flag_6_to_52_bit0}==0$$

Similarly L2B ocean products can be quality filtered following the “Ocean_products_quality_flag” included into the AMSR-E L2B products. These are:

Ocean Summary Quality Flag



The Ocean_summary_quality_flag indicates one of several conditions for each scan. In the event that more than one of the conditions are true, the flag will contain the lowest numerical value of the conditions that are true.

Ocean Summary Quality Flag Values

Value	Definition
0	Good scan
1	Bad calibration data
2	Bad scan as identified by the scan summary bit in the Scan_quality_flag
3	Bad time information based on Level-2A san summary flag

The Ocean_products_quality_flag is an array of six bytes for each observation of each scan and are described herebelow:

Byte One

The first byte of the Ocean_products_quality_flag describes the possibility of ice based on climatology, and the general plausibility of the observed brightness temperatures

Byte Two of the Ocean Products Quality Flag provide the *acceptability of products at a given resolution*. There is one flag for each resolution in the products

Very Low resolution (VeryLowres_flag),
 Low resolution (Lowres_flag),
 Medium resolution (Mediumres_flag) and,
 High resolution (Highres_flag)

Byte three of the Ocean Products Quality Flag: *proximity and intensity of rain*

Bite

0 No rain contamination
 16 Light rain in cell
 20 Light rain within 25 km of cell
 24 Very light rain within 25 km of cell
 30 Light rain within 40 km of cell
 31 Very light rain within 40 km of cell

In the present version of the algorithm, the rain flag is not used to keep as much data as possible.

Byte four of the Ocean_products_quality_flag indicates the *surface type based on the fraction of land* for three different spatial resolutions. It is referred to as "Land_flag". based on the fraction of land for three different spatial resolutions.

Bite	Resolution	Value	Definition
0-1	Very low	0	0 to 0.2%
2-3	Low	1	0.2% to 1.4% land
4-5	Medium	2	More than 1.4% land



6-7	n/a
-----	-----

Byte Five

The fifth byte of the Ocean_products_quality_flag is an unsigned integer representing the sun glint angle, which is the angle between the spacecraft viewing vector and the sun's specular reflection vector. Because of the possibility of clipping, an angle of 127.5 should be interpreted as 127.5 degrees or greater.

Radio Frequency Interference (RFI) from a variety of sources has been identified as an ongoing and increasing source of contamination affecting channels 10.7 GHz and 18.7 GHz (both h-pol and v-pol) during the descending pass of the AMSR-E satellite. Beginning with the launch of AMSR-E in 2002, RFI from the Hotbird and Astra satellites was identified as the primary source of contamination in the 10.7 GHz channel. A flag was then implemented to identify and exclude the impacted observations, such as swath and wind data at low geostationary RFI angles. Since 2007, interference due to HDTV broadcasting activities has been identified as the primary source of RFI, which impacts the AMSR-E 18.7 GHz channel. The locations of interference are geometrically consistent with geosynchronous satellite signals reflecting off the ocean surface into AMSR-E's field of view, and the timing of the interference is coincident with the launch of HDTV satellites, such as DirecTV-10 in 2007 and DirecTV-11 in 2008. In addition, spot beams used by HDTV satellites to serve different local programming to different local markets (and thus reuse the same set of frequencies), have resulted in amplified RFI. Since spot beams cover nearly the entire U.S. coastline, data users should be aware that AMSR-E ocean products derived from descending 18.7 GHz observations are potentially impacted along all U.S. coastal waters from September 2007 forward. As RFI interference continues to be an issue, updates to the science algorithm to flag and exclude all sources of RFI contamination are ongoing. In addition, the AMSR-E ocean products now include an RFI angle grid as a parameter for determining glint angles. Byte 6 is an unsigned integer representing the RFI glint angle, which is the angle between the spacecraft viewing vector and some of the previously listed geostationary satellite specular RFI reflection vector. Because of the possibility of clipping, an angle of 127.5 should be interpreted as 127.5 degrees or greater. The associated flag is named "RFI_glint_angle".

We therefore filter the input L2B water vapor (WV), Cloud liquid water (CLW) and 10 m height surface wind speed (U_{10}) products following

1. Land_flag=0
2. VeryLowres_flag=0 & Lowres_flag=0 & Mediumres_flag=0 & Highres_flag=0
3. RFI_glint_angle > 25
4. Ocean_summary_quality_flag=0



Note that no filter for sea ice is included as we consider only tropical regions and we keep all conditions of rain (in this first version of the ATBD).

4.4.2 Input Data re-gridding

The Level2B product grids are 720 rows by 1440 columns. Cell spacing is 0.25 degrees x 0.25 degrees. After filtering we therefore re-gridded all L2A data on this L2B rectangular grid using simple spatial bin averaging for L2A.

4.4.3 Surface specular V-pol brightness temperature at C- and X-band

Using L2B WV, CLW and U_{10} , re-gridded L2A and (CCI) SST data, the sea surface specular V-pol T_b are then estimated separately at both C and X band using (30) and the different terms of the RTM model components described previously :

$$T_{surf,f}^{spec} = T_S [1 - R_{V,f} - \Delta e_{o,f,V}(U_{10})]$$

4.4.4 Earth Incidence Variations

The surface emissivity also depends on the Earth Incidence Angle (EIA). Due to the oblateness of the Earth the EIA can deviate by about ± 0.5 degrees from the nominal EIA of 55 degrees over the course of an AMSR-E orbit. The method to compensate for the variation in EIA is frequency dependent and follows :

$$T_{surf,6.9}^{spec} = T_{surf,6.9}^{spec} - 2.9 (EIA - 55)$$

$$T_{surf,10.7}^{spec} = T_{surf,10.7}^{spec} - 2.7 (EIA - 55)$$

4.4.5 SST and Atmospheric corrections refinements

Additional empirical corrections are finally applied to correct for residual biases as a function of first SST and then columnar water vapor V and columnar cloud liquid content L . These empirical corrections were derived as follows for each C- and X- band frequency of AMSR-E. The specular sea surface emission was evaluated using CCI SST and CCI L-band -based SSS (v2.31) products as inputs to Equation (22) for 21 months from January 2010 to September 2011. The AMSR-E surface T_b s corrected for atmospheric effects including downwelling radiation scattering effects and corrected for the isotropic rough sea surface emission were evaluated using the previous RTM. These residual specular emission quantity were collected for all four regions together and binned as function of CCI SST. As found, after applying the full RTM corrections, residual systematic biases as a function of SST are found with differing behaviour at each electromagnetic frequency (see Figure 14).

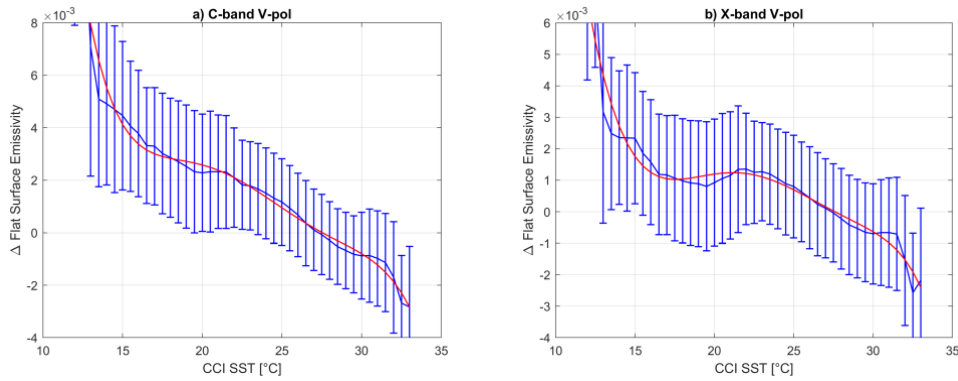


Figure 14: Residual Biases between estimated specular sea surface emission from AMSR-E and forward model estimates (based on CCI SSS and SST) as a function of CCI SST for C-band (left) and X-band (right) at V-polarized data. The blue curves are showing the median bias ± 1 STD as a function of the SST. The red curves are 6th-order polynomial fits.

After applying the previous RTM, the surface specular Tb are therefore corrected with an additional SST-dependent correction:

$$T_{surf,6.9}^{spec'} = T_{surf,6.9}^{spec} - \Delta T_{SST,6.9}^{adj}(T_s)$$

$$T_{surf,10.7}^{spec'} = T_{surf,10.7}^{spec} - \Delta T_{SST,10.7}^{adj}(T_s)$$

Where the $\Delta T_{SST,f}^{adj}(T_s)$ are 6th-order polynomial functions of the SST, which were derived by fitting observed residual biases (see Figure 14):

$$\Delta T_{SST,f}^{adj}(T_s) = T_s \sum_{i=0}^6 c_{i,f} \cdot T_s^i$$

The coefficients $c_{i,f}$ for C- and X-band frequencies are given in the following table:

$c_{i,f}$	f=6.9 GHz	F=10.7 GHz
i=0	0.5186	0.1691
i=1	-0.1191	-0.0266
i=2	0.0111	9.5888e-04
i=3	-5.2418e-04	5.3752e-05
i=4	1.3158e-05	-5.0486e-06



i=5	-1.6187e-07	1.3794e-07
i=6	7.1766e-10	-1.3016e-09

After correcting for residual biases in SST, residual biases as function of both columnar water vapor V and columnar cloud liquid content L were found (see Figure 15). We therefore further correct the SST-corrected surface $T_{surf,f}^{spec'}$ using:

$$T_{surf,6.9}^{spec''} = T_{surf,6.9}^{spec'} - \Delta T_{atm,6.9}^{adj}(V, L)$$

$$T_{surf,10.7}^{spec'} = T_{surf,10.7}^{spec'} - \Delta T_{atm,10.7}^{adj}(V, L)$$

Where the $\Delta T_{atm,f}^{adj}(V, L)$ are bivariate polynomial corrections:

$$\Delta T_{atm,f}^{adj}(V, L) = \sum_{i=0}^6 \sum_{j=0}^{6-i} d_{i,j,f} V^i L^j$$

Where V and L are the columnar water vapour (in [mm]) and the cloud liquid content (in kg/m^3), respectively.

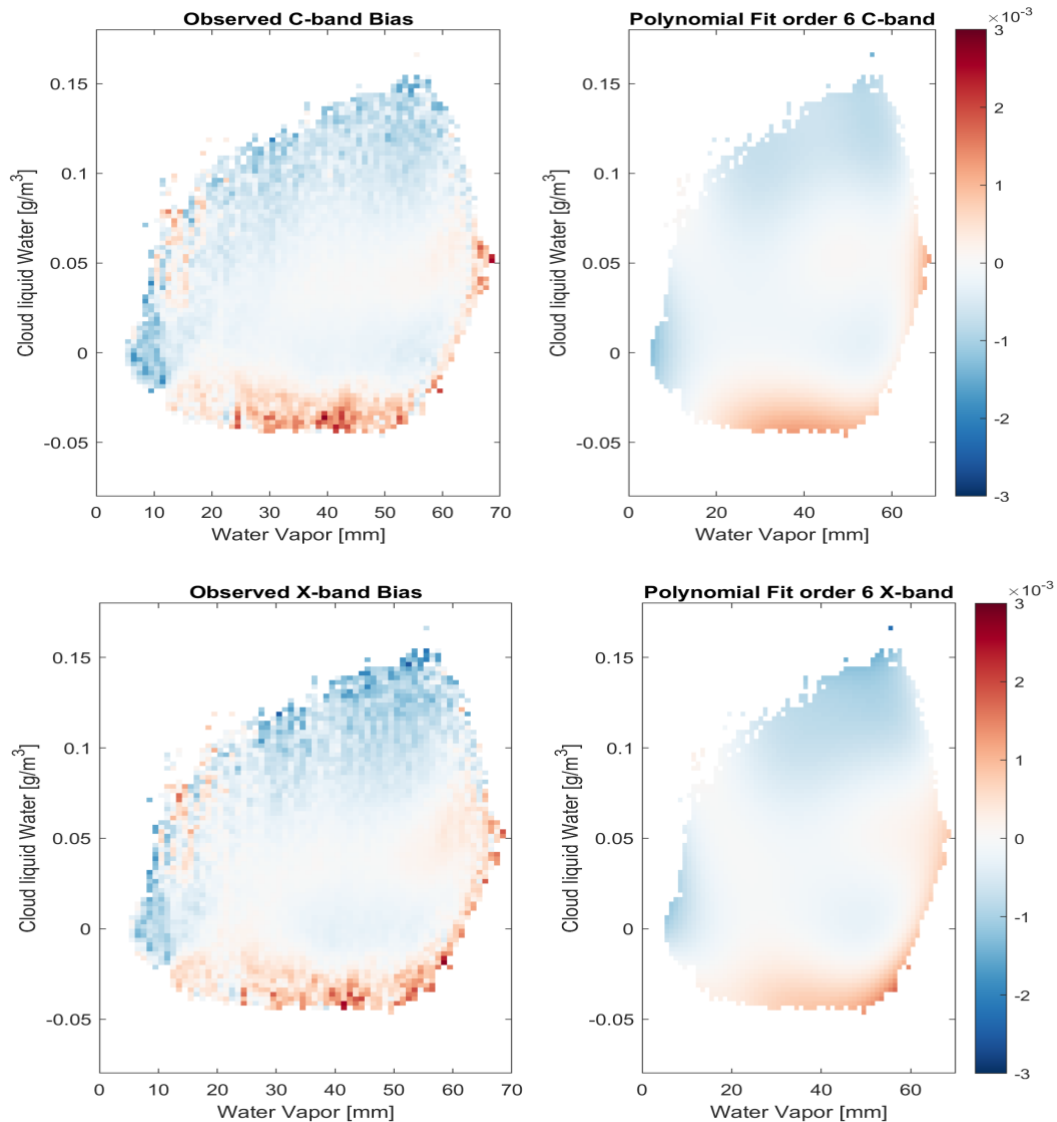


Figure 15: Observed (left plots) and modeled (right plots) residual biases as a function of both columnar Water Vapor (V) and Cloud liquid water (L). Top and bottom panels are for C- and X- band corrections, respectively.

Note that the range of valid values for the AMSR-E L2B cloud liquid water content is -0.05 to 2.45 mm. REMSS use a small negative offset to account for random noise in the data. In clear sky conditions, all cloud values should be zero. However, there is some noise inherent in the data. So in practice, clear sky values average zero. Some are a little above and some are a little below zero. Clear sky values that land a little below zero are kept so that they average out with the clear sky values that land a little above zero. If one set negative cloud retrievals to zero, then it would tend to push the average a little too high. Note that the correction is most important for clear sky conditions ($L < 0$) and strong water vapour.

The 28 polynomial coefficients $d_{i,j,f}$ are given herebelow for each frequency:



Climate Change Initiative+ (CCI+)
Phase 2
 Algorithm Theoretical
 Development Basis Document

Ref.: ESA-CCI-PRGM-EOPS-SW-17-0032
 Date: 15/07/2023
 Version : v4.0
 Page: 69 of 87

$d_{i,j,f}$	f=6.9 GHZ	F=10.7 GHz
i=0,j=0	-0.0022	-0.0014
i=0,j=1	-0.0181	-0.0811
i=0,j=2	0.7813	1.4239
i=0,j=3	-0.0916	-4.1525
i=0,j=4	-73.6988	-55.1092
i=0,j=5	755.6296	921.0287
i=0,j=6	-3.3162e+03	-4.1704e+03
i=1,j=0	2.2718e-04	8.1722e-05
i=1,j=1	0.0037	0.0121
i=1,j=2	-0.0791	-0.1432
i=1,j=3	0.0238	0.2447
i=1,j=4	1.2992	-0.5798
i=1,j=5	5.8124	6.8483
i=2,j=0	-6.9924e-06	1.8660e-06
i=2,j=1	-2.7975e-04	-6.7317e-04
i=2,j=2	0.0038	0.0061
i=2,j=3	-0.0078	-0.0083
i=2,j=4	-0.0249	0.0011

i=3,j=0	-6.4174e-08	-2.3399e-07
i=3,j=1	7.7236e-06	1.5979e-05
i=3,j=2	-6.7072e-05	-1.0807e-04
i=3,j=3	1.0365e-04	4.8352e-05
i=4,j=0	8.1096e-09	6.6315e-09
i=4,j=1	-8.1112e-08	-1.5401e-07
i=4,j=2	4.0436e-07	7.3521e-07
i=5,j=0	-1.6668e-10	-9.0218e-11
i=5,j=1	2.2051e-10	3.7474e-10
i=6,j=0	1.1178e-12	5.3490e-13

4.4.6 Land Sea Contamination filtering and Outliers Removal

4.4.6.1 Land Sea Contamination filtering

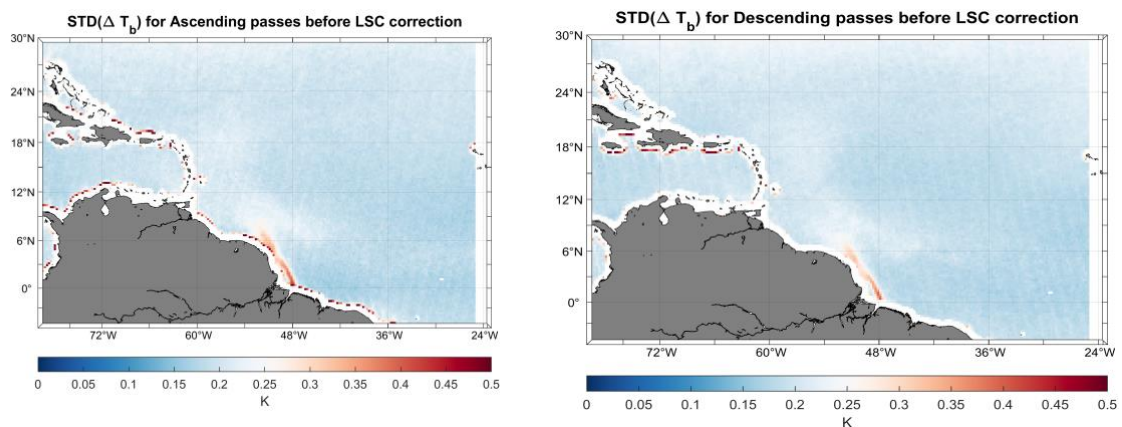


Figure 16: Standard deviation of the surface brightness temperature contrast in Ascending (left) and Descending (right) passes evaluated over the AORP region and the period 07/2002 to 11/2011.

As illustrated in Figure 16 for the specific case of the AORP region, we found that the standard deviation of the surface brightness temperature contrast evaluated over the period 07/2002 to

11/2011 do not show the same spatial patterns in Ascending (left) and Descending (right) passes. The temporal Median Absolute Deviation (MAD) of the differences between A and D passes are high up to ~140 km from the nearest coasts with a high standard deviation, before converging to similar values more than 140 km offshore where the salinity signal variability is detected. Similar along coasts differences in the A and D signals were found for the three others regions. The > 0.3K differences between A and D tracks near the coast would correspond to > 6 pss signals, which are way larger than those induced by a potential diurnal SSS cycle in the studied regions, and thus very likely linked to land contamination. MAD maps for A and D passes calculated from the entire AMSR-E database shows that A and D brightness temperatures display extreme values at different locations, always situated downstream of the coast when following the satellite track. These outliers in brightness temperature are thus most likely associated with contamination by land signals.

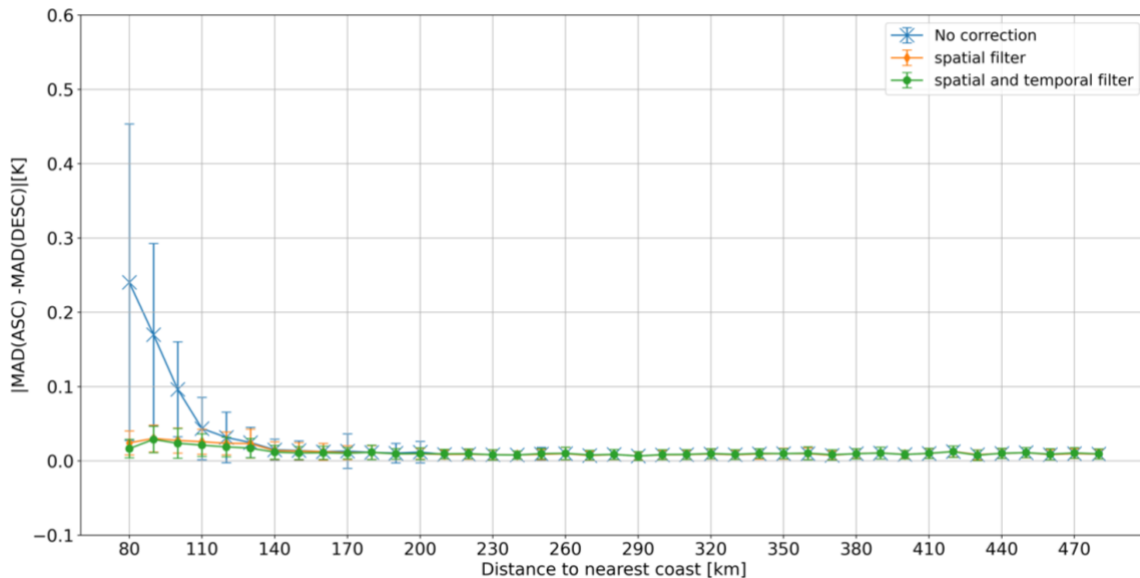


Figure 17: Means and standard deviation of the absolute difference of the Median Absolute Deviation (MAD) between ascending (A) and descending (D) brightness temperature in function of the distance to the nearest coast [in km] in the Bay of Bengal. In blue the mean before filtering the land-sea contamination, in orange the mean on the spatial filtered data and in green the mean on the spatial and temporal filtered data.

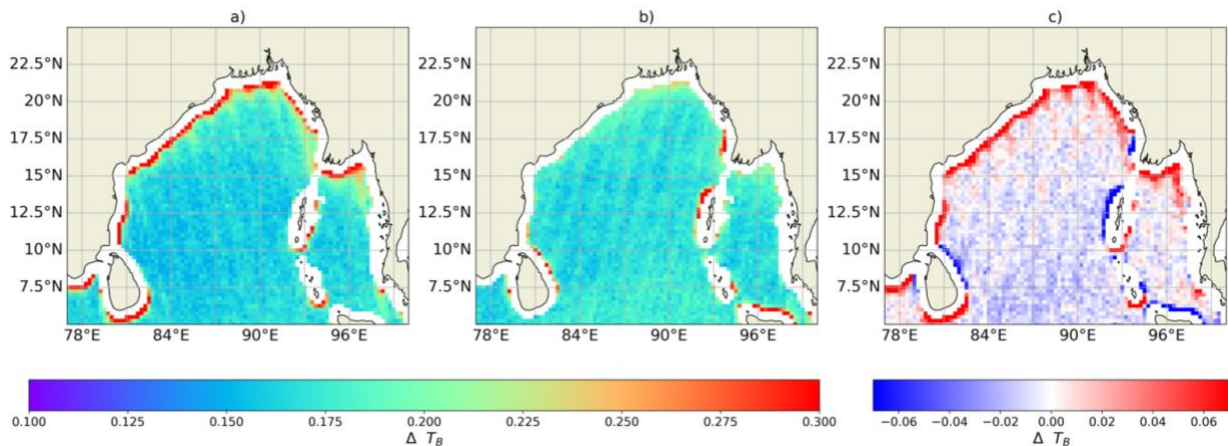


Figure 18: Temporal Median Absolute Deviation of the brightness temperature contrast between X- and C-band from all 2002-2011 AMSR-E data for a) ascending (A) and b) descending (D) satellite passes and c) for their difference.

To filter this land-sea contamination, we apply a spatial filter by removing data which show higher MAD in one pass direction than in the other. To this aim, we defined a mask where the difference of the temporal MAD for ascending data is greater than +0.06K (equivalent of 1.2 psu) and for the descending data where the difference is less than -0.06 K, creating two static masks applied separately for ascending and descending brightness temperature data (see Figure 18). After applying such filter (see Figure 17), the variations of the MAD decreases consistently, indicating a clear attenuation of the land impact on the brightness temperature.

4.4.6.2 Remaining outlier filtering

Once the land contamination mask has been applied, we scan the remaining ΔT_B time series at each location to exclude potential outliers such as the one from unfiltered Radio Frequency Interferences. The temporal median and Mean Absolute Deviation (MAD) of ΔT_B is re-evaluated in $\frac{1}{4}^\circ \times \frac{1}{4}^\circ$ boxes, separately for A and D direction, over May 2002-October 2011. Outliers (more than 3 MAD away from the median) are then filtered out. After these two filtering steps, the difference in the MAD of the A and D passes is less than 0.02K (0.4 psu) (Figure 17, green curve).

AMSR-E data are collected and processed for each day of a given month and then temporally averaged to provide monthly averaged median SSS fields. Prior averaging, it is important to remove remaining (after the quality filters described previously) outliers in the time series. We used the 21 months from January 2010 to October 2011 to estimate static spatial maps of the median absolute temporal deviation (MAD) of the specular sea surface emissivity frequency differential contrasts Δe_{surf}^{spec} for each of the 4 regions. An outlier is defined as an element that is

greater than 3 scaled median absolute deviation (MAD) away from the median. The scaled MAD is defined as

$$MAD(\Delta T_{surf}^{spec}) = K \cdot MEDIAN(|\Delta T_{surf}^{spec} - MEDIAN(\Delta T_{surf}^{spec})|)$$

where K is the scaling factor and is approximately 1.4826.

4.4.7 Neural Network SSS inversion

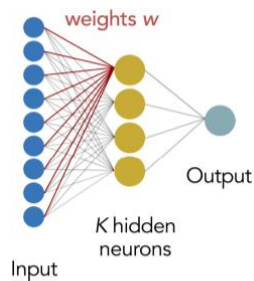
4.4.7.1 Neural Network training

In each region, 21 monthly maps of CCI SSS v3.2 data from January 2010 to September 2011 were used to train a two layer feed-forward neural network (NN) with 40 Neurones per layers. A Bayesian regularization backpropagation technique is used to minimize a linear combination of squared errors and weights. It also modifies the linear combination so that at the end of training the resulting NN has good generalization qualities. Backpropagation uses the Jacobian for calculations with a mean of squared errors performance function.

The input data to the NN training are the following 6 parameters:

- The monthly averaged estimated $\Delta\epsilon$ flat surface emissivity difference between the C-X bands (corrected for atmospheric, celestial, roughness effects, LSC contamination and outliers),
- The monthly averaged AMSR-E SST, CLW, WV and SWS, and, the,
- SSS from CCI,

4.4.7.2 Neural Network functions



Network architecture

Figure 19: Neural Network architecture



For each region, the Neural Network functions determined from the NN training have the following shape using as input Δe , SST, CLW, SWS and WV:

$$SSS_{NN} = \frac{(N_{NN} - b_{SSS})}{a_{SSS}}$$

where

$$N_{NN} = W_2 \cdot A_2 + B_3$$

with

$$A_2 = \frac{2}{(1 + \exp(-2 \cdot n_2))} - 1$$

and

$$n_2 = W_1 \cdot A_1 + B_2$$

$$A_1 = \frac{2}{(1 + \exp(-2 \cdot n_1))} - 1$$

and

$$n_1 = I_W \cdot P_n + B_1$$

Where

$$P_n = \begin{bmatrix} a_1 \cdot \Delta e + b_1 \\ a_2 \cdot sst + b_2 \\ a_3 \cdot clw + b_3 \\ a_4 \cdot sws + b_4 \\ a_5 \cdot wv + b_5 \end{bmatrix}$$

where

- $a_{i=1,\dots,5}$, $b_{i=1,\dots,5}$, a_{SSS} and b_{SSS} are single coefficients,
- I_W and W_1 are 40×5 and 40×40 matrices, respectively,
- B_1 , B_2 , and W_2 are 1×40 vectors,

of numerical coefficients which depend on the selected river plume region.



4.4.8 References for AMSR-E SSS algorithm

ID	Document	Reference
RD01	Reul Nicolas, Saux Picart Stephane, Chapron Bertrand, Vandemark D., Tournadre Jean, Salisbury J. (2009). Demonstration of ocean surface salinity microwave measurements from space using AMSR-E data over the Amazon plume. <i>Geophysical Research Letters (GRL)</i> , 36, 1-5 .	https://doi.org/10.1029/2009GL038860
RD02	Qingtao Song and Zhaohui Wang. (2017). Sea surface salinity observed from the HY-2A satellite. <i>Satellite Oceanography and Meteorology</i> , vol.2 (1): 41–48.	http://dx.doi.org/10.18063/SOM.2017.01.004 .
RD03	Meissner T., and F.J. Wentz, (2004) The Complex Dielectric Constant of Pure and Sea Water From Microwave Satellite Observations, <i>IEEE TRANSACTIONS ON GEOSCIENCE AND REMOTE SENSING</i> , VOL. 42, NO. 9	
RD04	Merchant, C.J., Embury, O., Bulgin, C.E., Block T., Corlett, G.K., Fiedler, E., Good, S.A., Mittaz, J., Rayner, N.A., Berry, D., Eastwood, S., Taylor, M., Tsushima, Y., Waterfall, A., Wilson, R., Donlon, C. Satellite-based time-series of sea-surface temperature since 1981 for climate applications, <i>Scientific Data</i> 6:223 (2019).	http://doi.org/10.1038/s41597-019-0236-x
RD05	Good, S.A.; Embury, O.; Bulgin, C.E.; Mittaz, J. (2019): ESA Sea Surface Temperature Climate Change Initiative (SST_cci): Level 4 Analysis Climate Data Record, version 2.1. Centre for Environmental Data Analysis, 22 August 2019. doi:10.5285/62c0f97b1eac4e0197a674870afe1ee6.	http://dx.doi.org/10.5285/62c0f97b1eac4e0197a674870afe1ee6
	Meissner, T. and F.J. Wentz, (2012), The Emissivity of the Ocean Surface Between 6 - 90 GHz Over a Large Range of Wind Speeds and Earth Incidence Angles, <i>IEEE Transactions on Geoscience and Remote Sensing</i> , 50(8), 3004-3026.	
RD04	Wentz, F. J. and T. Meissner, (2016), Atmospheric Absorption Model for Dry Air and Water Vapor at Microwave Frequencies below 100 GHz Derived from Spaceborne Radiometer Observations, <i>Radio Science</i> , 51, 381-391.	
RD05	Rodgers, C. D. (1976). Retrieval of atmospheric temperature and composition from remote measurements of thermal radiation. <i>Reviews of Geophysics</i> , 14(4), 609.	
RD06	C. S. Cox, "Measurements of slopes of high frequency wind waves," <i>J. Mar. Res.</i> , vol. 16, pp. 199–225, 1958.	
RD07	H. Mitsuyasu and T. Honda, "Wind-induced growth of water waves," <i>J. Fluid Mech.</i> , vol. 123, pp. 425–442, 1982	
RD08	Rodgers, C. D. (1990). Characterization and error analysis of profiles retrieved from remote sounding measurements. <i>Journal of Geophysical Research</i> , 95(D5), 5587.	
RD09	P. M. Smith, "The emissivity of sea foam at 19 and 37 GHz," <i>IEEE Trans. Geosci. Remote Sensing</i> , vol. GE-26, pp. 541–547, Sept. 1988.	
RD10	W. C. Keller and J. W. Wright, "Microwave scattering and the straining of wind-generated waves," <i>Radio Sci</i> , vol. 10, pp. 139–147, 1975.	



Climate Change Initiative+ (CCI+)
Phase 2
Algorithm Theoretical
Development Basis Document

Ref.: ESA-CCI-PRGM-EOPS-SW-17-0032
 Date: 15/07/2023
 Version : v4.0
 Page: 76 of 87

ID	Document	Reference
RD11	M. L. Banner and I. R. Young, "Modeling spectral dissipation in the evolution of wind waves. Part I: Assessment of existing model performance," J. Phys. Oceanography, vol. 24, pp. 1550–1571, 1994.	
	<p>P. A. Hwang, D. W. Wang, E. J. Walsh, W. B. Krabill, and R. N. Swift, "Airborne measurements of the wavenumber spectra of ocean surface waves. Part I: Spectral slope and dimensionless spectral coefficient," J. Phys. Oceanography, vol. 30, pp. 2753–2767, 2000.</p> <p>P. A. Hwang and D. W. Wang, "Directional distributions and mean square slopes in the equilibrium and saturation ranges of the wave spectrum," J. Phys. Oceanography, vol. 31, pp. 1346–1360, 2001.</p> <p>V. G. Irisov, 2000, Azimuthal variations of the microwave radiation from a slightly non-Gaussian sea surface Radio Science, Volume 35, Number 1, Pages 65–82.</p> <p>S. H. Yueh, "Directional signals in Windsat observations of hurricane ocean winds," IEEE Transactions on Geoscience and Remote Sensing, vol. 46, no. 1, pp. 130-136, 2008.</p> <p>S. H. Yueh, W. Wilson, S. J. Dinardo, and F. K. Li, "Polarimetric microwave brightness signatures of ocean wind directions," IEEE Transactions on Geoscience and Remote Sensing, vol. 37, no. 2, pp. 949-959, 1999.</p> <p>Meissner, Thomas and Wentz, Frank J., "Ocean retrievals for WindSat: Radiative transfer model, algorithm, validation," presented at the 9th Specialist Meeting on Microwave Radiometry and Remote Sensing Applications, Puerto Rico, USA, 2006, Paper Catalog # 06EX1174C. [Online]. Available: http://www.remss.com/papers/meissner_and_wentz(2006).pdf.</p> <p>S. H. Yueh, W. J. Wilson, S. Dinardo, and F. K. Li, "Polarimetric microwave brightness signatures of ocean wind directions," IEEE Trans. Geosci. Remote Sens., vol. 37, no. 2, pp. 949–959, Mar. 1999.</p> <p>J. R. Piepmeier and A. J. Gasiewski, "High-resolution passive polarimetric microwave mapping of ocean surface wind vector fields," IEEE Trans. Geosci. Remote Sens., vol. 39, no. 3, pp. 606–622, Mar. 2001.</p> <p>S. H. Yueh, W. Wilson, S. Dinardo, and S. V. Hsiao, "Polarimetric microwave wind radiometer model function and retrieval testing for WindSat," IEEE Trans. Geosci. and Remote Sensing, vol. 44, no. 3, pp. 584– 596, Mar. 2006.</p>	



5 Conclusions and way forward for AMSR-E SSS algorithm

Most of the AMSR-E SSS retrieval algorithm have been developed and tested. So far, we have tested NN with 2 hidden layers and 40 Neurons per layers using as input data the surface emissivity frequency differential contrasts after atmospheric corrections and the extra polynomial empirical adjustments (wind, sst, clw, wv). Retrieval tests will be conducted with or without these extra polynomial empirical adjustments to determine in which conditions do the NN inversion performs better. As found, one of the remaining issue is the relatively low number of training observations for the freshest SSS (due in part to low coverage of fresh waters and LSC filtering) which lead to overestimation of SSS from AMSR-E in the freshest SSS zones. To better characterize these conditions, the distance to coast might be used as an input to the NN. An additional task will finally be to develop an error estimate for the AMSR-E SSS retrievals. Validation procedures will include in situ SSS data (Argo, TSG, XBT and moorings) gathered over the four regions back to 2002.



Climate Change Initiative+ (CCI+)
Phase 2
Algorithm Theoretical
Development Basis Document

Ref.: ESA-CCI-PRGM-EOPS-SW-17-0032
Date: 15/07/2023
Version : v4.0
Page: 78 of 87



Appendix A - L2P algorithms

A.1 Introduction

CCI L2 products are Level 2 Pre-Processed (L2P) products defined in the CCI data standards document (AD.9).

Table A-1: L2P definition extracted from processing level of CCI Data Standards document [AD.9].

Level	<Processing Level> Code	Description	Based on Source
Level 2 Pre-processed	L2P	Geophysical variables derived from Level 1 source data at the same resolution and location as the level 1 data, typically in a satellite projection with geographic information. These data form the fundamental basis for higher level CCI products.	GHR SST

L2P files are daily files with ascending/descending orbit separation and are available for both SMOS and SMAP sensors.

The main content of L2P products are SSS from SMOS or SMAP. SSS is corrected from different systematic errors, as land-sea contamination systematic errors and latitudinal systematic errors, as outputs of the Level4 CCI SSS data version 3 chain (last release of the phase 1).

L2P products are used only for internal validation and are not distributed to external users.

A.2 Method

A.2.1 Input Data re-gridding

While the SMOS Level 2 data are provided onto the EASE grid at 25 km resolution, the SMAP Level 2 data is not given on that grid. A first step therefore consists in projecting SMAP SSS onto the EASE grid at 25 km resolution. A closest neighbour interpolation scheme is used for that purpose.

A.2.2 L2P variables definition

SSS

The sea surface salinity in L2P files is unbiased: it is corrected from land-sea contamination systematic errors and seasonal latitudinal systematic errors. For SMOS, the SSS is also corrected from rain rate by using A. Supply relation which gives the SSS freshening according to the



instantaneous rain rate. This formula is not applicable to SMAP data. For SMOS rain rate larger than 10 mm/h, the SSS is not corrected from rain rate and put to NaN. For SMAP rain rate larger than 0.5 mm/h, the SSS is put to NaN.

$$sss = sss_uncorrected + sss_correction$$

Where $sss_uncorrected$ is SSS from input data described in section 2.1.2 and $sss_correction = -sss_bias$.

SSS random uncertainties

The random error of SSS, sss_random_error , is the theoretical error and it is estimated as follows for SMOS and SMAP.

L2P SMOS

The random error of SMOS SSS is estimated as follow (see E3UB for more details):

$$sss_random_error = eSSS \times error_factor \times Chi$$

Where $eSSS$ and Chi are outputs from SMOS L2OS processor, and represent the 'theoretical error' and the retrieval Chi , respectively. The $error_factor$ parameter depends on the distance from the nearest coast $dmin$ and is estimated as follow:

$$error_factor = p1 \times \left(\frac{dmin}{1000}\right)^3 + p2 \times \left(\frac{dmin}{1000}\right)^2 + p3 \times \frac{dmin}{1000} + p4$$

With: $p1=-1.773 \cdot 10^{-11}$; $p2=1.025 \cdot 10^{-7}$; $p3=-2.057 \cdot 10^{-4}$; $p4=1.140$ and $dmin$ is the distance from the coast expressed in km.

L2P SMAP

The random error of SMAP SSS is as follow:

$$sss_random_error = \frac{0.38}{0.015 \times SST + 0.25} \times error_factor$$

Where $error_factor$ has been determined based on observed errors derived from internal consistency comparisons and depends on the distance from the coast $dmin$ and is estimated as follow:

$$error_factor_smap = p1 \times \left(\frac{dmin}{1000}\right)^8 + p2 \times \left(\frac{dmin}{1000}\right)^7 + p3 \times \left(\frac{dmin}{1000}\right)^6 + p4 \times \left(\frac{dmin}{1000}\right)^5 + p5 \times \left(\frac{dmin}{1000}\right)^4 + p6 \times \left(\frac{dmin}{1000}\right)^3 + p7 \times \left(\frac{dmin}{1000}\right)^2 + p8 \times \frac{dmin}{1000} + p9$$

$p1=0.002991909878747$; $p2=-0.057895699052765$; $p3=0.454231563716574$;



p4=-1.869918681721869; p5=4.369867374935416; p6=-5.877381371897917;
p7=4.439753964071140; p8=-1.785811244191490; p9=1.353937878613555;

SSS systematic errors

sss_bias is estimated from L4 data products (Cf. 4.3) and is defined as follows:

$$\text{sss_bias} = \text{sss}_{\text{uncorrected}} - \text{SSS}$$

Flag computation

Three flags are defined for L2P SSS and described hereafter:

SSS quality check

sss_qc = 0 for good pixels and sss_qc=1 for bad pixels.

A bad pixel is a pixel associated with SSS values verifying the following condition:

$$|\text{sss} - \text{SSS_monthly_L4}| > 3 \sigma$$

Where $\sigma = \sqrt{\text{sss_random_error}^2 + \text{weekly_variability} + \text{sss_random_error_L4}^2}$

σ combines the random error on the L2P SSS, the random error on L4 salinity and the weekly natural variability (corresponding to the representativity error between monthly and weekly SSS fields used in L4 processing).

This condition means that L2P SSS (which is not averaged) should be comparable to the monthly SSS estimated in L4 in a range of 3 times the natural variability and the measurement error.

Land-sea quality check

L2P lsc_qc is computed in the same way than for L4 (section 0).

Ice-Sea quality check

The ice flag is the same than the one computed at L4 (section 0)

A.3 Conclusion

L2P products are used as inputs to Level 3 CCI+SSS products. These products have been designed as useful tools for investigating validation results obtained for L4 and/or L3 products.



Appendix B - L3C algorithms

B.1 Introduction

The level 3 (L3) products are, by definition, time and space-averaged products obtained sensor by sensor, without mixing inter-sensor information. Here, we consider simple averages of swath Level 2 SSS products, which may have been already corrected for some biases (e.g. land sea contamination or spatio-temporal drifts corrections). These products can thus be used as a reference in terms of observed SSS and of its variability as derived from each sensor. Indeed, we don't apply to the observed SSS any specific smoothing operation (for example, by introducing representativity errors or variance filtering).

L3C products are used only for internal validation and are not distributed to external users.

B.2 Input data for CCI+SSS L3 data

B.2.1 SMOS and SMAP L2P products

SMOS and SMAP L3 products are computed from Level 2P CCI+SSS output. These products are the swaths L2P SMOS and SMAP data generated by the algorithms described in section 2.

B.2.2 Aquarius Level 3 products

For Aquarius, we use as input the official release products L3 v5.0, which is the official end of mission public data release from the AQUARIUS/SAC-D mission (with DOI: 10.5067/AQR50-3SADS and which are accessible [here](#)). Aquarius Level 3 sea surface salinity standard mapped image data contains gridded 1 degree spatial resolution SSS averaged over daily, 7 day, monthly, and seasonal time scales. We use the daily non averaged dataset for generating the CCI+SSS L4 dataset V3. The ATBD for these Aquarius L3 products is detailed in [AD.4] and [AD.5] and therefore, not reproduced here.

B.3 CCI+SSS L3 product overview

CCI L3 products are Level 3 collated products (L3C).

Table B-1: L3C definition extracted from processing level of CCI Data Standards document [AD.9].

Level	<Processing Level> Code	Description	Based on Source
	L3C	Collated (L3C): Observations combined from a single instrument into a space-time grid.	

The L3 products contain the averaged SSS field and the associated error for each L-band sensor: SMOS, Aquarius, and SMAP.

There are three types of L3C products:

- L3C products with data averaged weekly on a daily sliding window, cumulating ascending and descending orbits;
- L3C products with data averaged monthly on a 15-day sliding window, cumulating ascending and descending orbits;
- L3C products with data averaged monthly on a 15-day sliding window for ascending and descending orbits separately;

The files' names indicate the date the time-composite are centred on. The weekly average is computed at the central date ± 3 days, every day, and the monthly average is computed at the central date ± 15 days every 1st and 15th of each month.

B.4 Method

B.4.1 Input Data re-gridding

While the L2P SMOS and SMAP data are already available on the EASE grid at 25 km resolution, Aquarius Level 3 products are not provided on that grid. A first step therefore consists in interpolating Aquarius SSS onto the EASE grid at 25 km resolution. A bilinear interpolation scheme is used for that purpose.

B.4.2 Input Data correction

As for SMOS and SMAP (Cf. 0), systematic errors corrections are applied to AQUARIUS L3 SSS resulting on the following systematic error estimation:

$$sss_bias = SSS_{uncorrected} - SSS$$

B.4.3 Data filtering

Before averaging the data over the corresponding period, SSS values are first filtered.

For SMOS, SSS values are filtered when :

- lsc_qc = 1;
- isc_qc = 1;
- ws > 16 m.s⁻¹;
- |Acard_model – Acard_measured | > 2;
- flag_many_outlier = 1;
- |sss – sss_window_median | > 3 × sss_random_error

sss_window_median is the median evaluated over the weekly or monthly time window used for averaging.

For SMAP, SSS values are filtered:

- According to the SMAP filtering criteria described in [AD10]
- When lsc_flag =1; or, when
- |sss – sss_window_median | > 3 × sss_random_error

For Aquarius, SSS values are filtered when:

- According to the Aquarius filtering criteria described in [AD10],
- When lsc_qc =1;
- When |sss – sss_window_median | > 3 × sss_random_error

B.4.4 L3C variables definition

SSS

Assuming that, for a given grid node and over the duration of a month (in case of monthly average) or a week (in case of weekly average), we have a set of level 2 salinities sss_i characterized by errors $sss_random_error_i^2$, then the weighted average salinity is obtained as follows:

$$sss_sensor = \frac{\sum_{i=1}^n \frac{sss_sensor_i}{sss_random_error_sensor_i^2}}{\sum_{i=1}^n \frac{1}{sss_random_error_sensor_i^2}}$$

i designates an individual measurement after filtering, n the number of individual measurements over the period (7days/30days) and sensor is either SMOS, SMAP, or Aquarius.

This average is calculated for each grid node and on a daily or a two-week temporal sliding window.

SSS random uncertainties

The random error associated with the averaged SSS is computed as follow:

$$\widetilde{\text{sss_random_error_sensor}} = \sqrt{\frac{1}{\sum_{i=1}^n \frac{1}{\text{sss_random_error_sensor}_i^2}}}$$

SSS systematic uncertainties

The systematic error associated with the averaged SSS is computed as follow:

$$\widetilde{\text{sss_bias_sensor}} = \frac{\sum_{i=1}^n \frac{\text{sss_bias_sensor}_i}{\text{sss_random_error_sensor}_i^2}}{\sum_{i=1}^n \frac{1}{\text{sss_random_error_sensor}_i^2}}$$

Flag computation

For quality check definition, we use monthly L4 salinities as a reference.

Weekly L3C

sss_qc = 0 for good pixels and sss_qc=1 for bad pixels.

A bad pixel is a pixel associated with SSS checking the following condition:

$$|\text{sss} - \text{SSS_monthly_L4}| > 3 \sigma$$

Where $\sigma = \sqrt{\text{sss_random_error}^2 + \text{weekly_variability} + \text{sss_random_error_L4}^2}$

sss_random_error_L4 is the random error on the L4 SSS.

Monthly L3C

sss_qc = 0 for good pixels and sss_qc=1 for bad pixels.

A bad pixel is a pixel associated with SSS checking the following condition:

$$|\text{sss} - \text{SSS_monthly_L4}| > 3 \sigma$$

Where $\sigma = \sqrt{\text{sss_random_error}^2 + \text{sss_random_error_L4}^2}$



Number of L4 outliers

The number of L4 outliers corresponds to the number of SSS rejected in L4 for an individual sensor. It is estimated as the occurrence over a temporal window of SSS values such as:

$$|sss - SSS_monthly_L4| > 3 \sigma$$

$$\text{Where } \sigma = \sqrt{sss_random_error^2 + weekly_variability + sss_random_error_L4^2}$$

Number of observations

Total_nobs corresponds to the number of Level 2 observations on the temporal window, used to compute the average L3 SSS, after the filtering explained in B.4.3.

B.5 Conclusion

L3C products are intended as a tool to interpret results obtained with L4 products: if two sensors see consistent SSS variability that is similar to SSS L4 observation, it is an indication of reliability of L4 SSS. Contrarily, if L4 SSS appears dubious and that the SSS from two sensors are very different, this could help to interpret where the dubious observation comes from. L3 products are not used as inputs to the algorithm used to generate L4 CCI+SSS products, as their quality checks remain peculiar to each sensor contrarily to what is performed for deriving L4 products. For example, if L4 filters retain only dubious data, this could be retrieved from L3C data.



Climate Change Initiative+ (CCI+)
Phase 2
Algorithm Theoretical
Development Basis Document

Ref.: ESA-CCI-PRGM-EOPS-SW-17-0032
Date: 15/07/2023
Version : v4.0
Page: 87 of 87

End of Document